NAVAL POSTGRADUATE SCHOOL

MONTEREY, CALIFORNIA

THESIS

A CFD ANALYSIS OF THE PERFORMANCE OF PIN-FIN LAMINAR FLOW MICRO/MESO SCALE HEAT EXCHANGERS

by

Sotirios Dimas

September 2005

Thesis Advisor: Ashok Gopinath
Co-Advisor: Jose O. Sinibaldi

THIS PAGE INTENTIONALLY LEFT BLANK

REPORT DOCUMENTATION PAGE			*Form Approved OMB No. 0704-0188*
Public reporting burden for this collection of information is estimated to average 1 hour per response, including the time for reviewing instruction, searching existing data sources, gathering and maintaining the data needed, and completing and reviewing the collection of information. Send comments regarding this burden estimate or any other aspect of this collection of information, including suggestions for reducing this burden, to Washington headquarters Services, Directorate for Information Operations and Reports, 1215 Jefferson Davis Highway, Suite 1204, Arlington, VA 22202-4302, and to the Office of Management and Budget, Paperwork Reduction Project (0704-0188) Washington DC 20503.			
1. AGENCY USE ONLY *(Leave blank)*	**2. REPORT DATE** September 2005	**3. REPORT TYPE AND DATES COVERED** Engineer's and Master's Thesis	
4. TITLE AND SUBTITLE: A CFD Analysis of The Performance of Pin-Fin Laminar Flow Micro/Meso Scale Heat Exchangers			**5. FUNDING NUMBERS**
6. AUTHOR(S) Sotirios Dimas			
7. PERFORMING ORGANIZATION NAME(S) AND ADDRESS(ES) Naval Postgraduate School Monterey, CA 93943-5000			**8. PERFORMING ORGANIZATION REPORT NUMBER**
9. SPONSORING /MONITORING AGENCY NAME(S) AND ADDRESS(ES) N/A			**10. SPONSORING/MONITORING AGENCY REPORT NUMBER**
11. SUPPLEMENTARY NOTES The views expressed in this thesis are those of the author and do not reflect the official policy or position of the Department of Defense or the U.S. Government.			
12a. DISTRIBUTION / AVAILABILITY STATEMENT Approved for public release; distribution is unlimited			**12b. DISTRIBUTION CODE** A

13. ABSTRACT (maximum 200 words)

A full three dimensional computational study was carried out using a finite-volume based solver for analyzing the performance of pin-fin based micro/meso scale heat exchangers with air as the working fluid. A staggered arrangement of cylindrical pin fins in rectangular channel geometry was used. Various configurations were considered consistent with a parallel experimental study being conducted based on a micro-wind tunnel setup. The pin/channel height used was 0.4 mm, and the pin diameters varied from 0.17-0.50 mm to give hydraulic diameters in the range of 0.13-0.78 mm. This gave volumetric area densities for the heat exchangers in the range of 5-15 mm2/mm3. Various heat exchanger configurations were simulated to determine performance characteristics such as the Nusselt number, friction factor, specific fluid friction power and Mach number in the Reynolds number regime for laminar flows. In addition a detailed numerical diagnosis was carried out to determine local behavior on the pin surfaces, end walls, etc to identify specific characteristics such as regions of high and low heat transfer, locations for possible shock formation, etc. The range of results obtained would be useful for future design of micro heat exchangers for use in small footprint, high heat flux dissipation applications like turbine blade and microelectronic systems.

14. SUBJECT TERMS Heat Exchanger, Compact, Computational Analysis, Micro Scale, Pin Fin Array			**15. NUMBER OF PAGES** 107
			16. PRICE CODE
17. SECURITY CLASSIFICATION OF REPORT Unclassified	**18. SECURITY CLASSIFICATION OF THIS PAGE** Unclassified	**19. SECURITY CLASSIFICATION OF ABSTRACT** Unclassified	**20. LIMITATION OF ABSTRACT** UL

NSN 7540-01-280-5500

Standard Form 298 (Rev. 2-89)
Prescribed by ANSI Std. 239-18

THIS PAGE INTENTIONALLY LEFT BLANK

Approved for public release; distribution is unlimited

A CFD ANALYSIS OF THE PERFORMANCE OF PIN-FIN LAMINAR FLOW MICRO/MESO SCALE HEAT EXCHANGERS

Sotirios Dimas
Lieutenant Junior Grade, Hellenic Navy
B.S., Hellenic Naval Academy, 1998

Submitted in partial fulfillment of the
requirements for the degree of

MECHANICAL ENGINEER

and

MASTER OF SCIENCE IN MECHANICAL ENGINEERING

from the

NAVAL POSTGRADUATE SCHOOL
September 2005

Author: Sotirios Dimas

Approved by: Ashok Gopinath
Thesis Advisor

Jose O. Sinibaldi
Co-Advisor

Anthony J. Healey
Chairman, Department of Mechanical Engineering

THIS PAGE INTENTIONALLY LEFT BLANK

ABSTRACT

A full three dimensional computational study was carried out using a finite-volume based solver for analyzing the performance of pin-fin based micro/meso scale heat exchangers with air as the working fluid. A staggered arrangement of cylindrical pin fins in rectangular channel geometry was used. Various configurations were considered consistent with a parallel experimental study being conducted based on a micro-wind tunnel setup. The pin/channel height used was 0.4 mm, and the pin diameters varied from 0.17-0.50 mm to give hydraulic diameters in the range of 0.13-0.78 mm. This gave volumetric area densities for the heat exchangers in the range of 5-15 mm2/mm3. Various heat exchanger configurations were simulated to determine performance characteristics such as the Nusselt number, friction factor, specific fluid friction power and Mach number in the Reynolds number regime for laminar flows. In addition a detailed numerical diagnosis was carried out to determine local behavior on the pin surfaces, end walls, etc to identify specific characteristics such as regions of high and low heat transfer, locations for possible shock formation, etc. The range of results obtained would be useful for future design of micro heat exchangers for use in small footprint, high heat flux dissipation applications like turbine blade and microelectronic systems.

THIS PAGE INTENTIONALLY LEFT BLANK

TABLE OF CONTENTS

LIST OF FIGURES

LIST OF TABLES

THIS PAGE INTENTIONALLY LEFT BLANK

NOMENCLATURE

A	Area $[\mathrm{m}^2]$
$\bar{A}$	Average array flow area $[\mathrm{m}^2]$
A_{wetted}	Flow wetted area $[\mathrm{m}^2]$
αH	Area magnification factor
α	Area density $[\mathrm{mm}^2/\mathrm{mm}^3]$
C_P	Specific heat capacity $\left[\mathrm{J}/\left(\mathrm{kg\,K}\right)\right]$
D	Pin fin diameter [m]
D_h	Hydraulic diameter [m]
E	Fluid friction power per unit area $[\mathrm{W}/\mathrm{m}^2]$
f	Friction factor
h	Heat transfer coefficient $\left[\mathrm{W}/\left(\mathrm{m}^2\,\mathrm{K}\right)\right]$
H	Pin height, distance between endwalls [m]
HX	Heat Exchanger
I	Turbulence intensity
k	Thermal conductivity $\left[\mathrm{W}/(\mathrm{m\,K})\right]$
k_t	Turbulence kinetic energy $[\mathrm{m}^2/\mathrm{s}^2]$
Kn	Knudsen number
L	Array length [m]
M	Mach number
$\dot{m}$	Mass flow rate [kg/s]
N_x	Number of streamwise pin fin rows
N_s	Number of spanwise pin fin rows
Nu	Nusselt number
NTU	Number of transfer units
P	Pressure [Pa]
Pr	Prandtl number

Q	Heat transfer rate [W]
Re	Reynolds number
S	Spanwise spacing between pin centers [m]
T	Temperature [K]
ΔT_{lm}	Log mean temperature difference [K]
U	Flow velocity [m/s]
V	Volume [m^3]
W	Array width [m]
X	Streamwise spacing between pin centers [m]
x^+	Thermal length scale
y^+	Turbulence length scale
ε	Heat exchanger effectiveness
ε_t	Turbulence dissipation rate [m^2/s^3]
ρ	Density [kg/m^3]
μ	Dynamic viscosity [Pa s]

ACKNOWLEDGMENTS

Without the exceptional guidance and assistance of my thesis supervisor, Professor Ashok Gopinath, it would not be possible to attain the completion of this work. I am truly grateful for his motivation.

I also want to thank Professor Jose Sinibaldi for his time and willingness to help me.

Most importantly I would like to thank my wonderful wife for her love, support and encouragement during the whole period of this research, and dedicate this thesis work to her, and to our lovely newborn daughter.

THIS PAGE INTENTIONALLY LEFT BLANK

I. INTRODUCTION

A. BACKGROUND-MOTIVATION

Today, great achievements and innovations are being made in the technological fields of microelectronics and micro-electromechanical (MEMS) systems. The demands for greater speed, more power, and less volume and mass have become more and more urgent in most of the forms and products of the science and technology. One of the undesirable consequences of this urgency is the operation in elevated temperatures. Since the systems tend to operate at higher energy levels, requirements are also emerging for the development of new devices that can remove the greater amounts of thermal energy and can dissipate the higher heat fluxes. The need for greater efficiencies and improved life cycles, which are combined with less thermal stresses, accelerated creep, and fatigue behaviors, is growing too.

Two of the most concerned industries are the microprocessor-microelectronics and the gas turbine industries. The former has concentrated its efforts on dramatically reducing the size and increasing the speed of its attainments. This resulted in higher functional temperatures, which create a severe operational condition with the significant effect of limiting the devices' life. So the heat removal process is critical and makes the interest in micro heat exchangers essential.

The gas turbine industry faces more severe conditions in which micro-exchanger technology could be more applicable, is mainly concerned with increased performance which translates to a higher inlet temperature. Because the turbine's reliability depends mostly on the mechanical behavior of the blades, their cooling due to increased performance is extremely vital. To increase the power, and thus the inlet temperature, the cooling techniques must be made more effective.

The current methods that had been used can be divided into external and internal. The external method is based on air film cooling by which air is injected through holes in the blade surface. The internal method is based on forced convection in which air is provided initially from the compressor bleed to the base (mounting) of the blade and then through an internal channel. A portion of the air can used for the film cooling, and some can be driven to a pin array, which would be seated at the trailing edge which is a suitable location (Ref. 1). The figure below presents schematically the two methods.

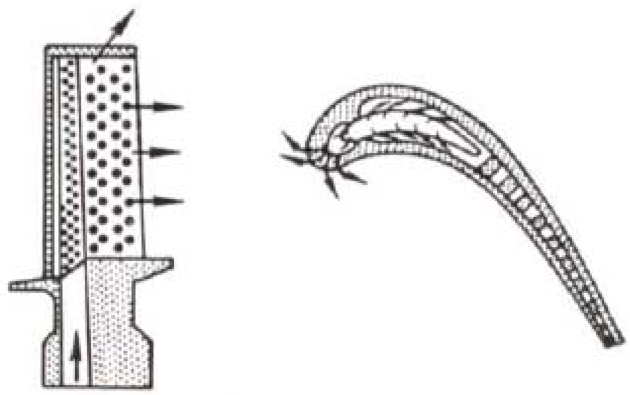

Figure 1. Cooled turbine airfoil with pin fins [from Metzger, 1984]

In addition to those two methods, other proposals include those that introduce air at the leading part of the blade, ribbed channels and impingement cooling techniques in order to increase the effectiveness of the heat removal process (Ref. 2). These two techniques dominated the research for almost two decades according to a literature review. The following figure shows two section cuts of a blade with the added characteristics, while the initial ones are kept parallel.

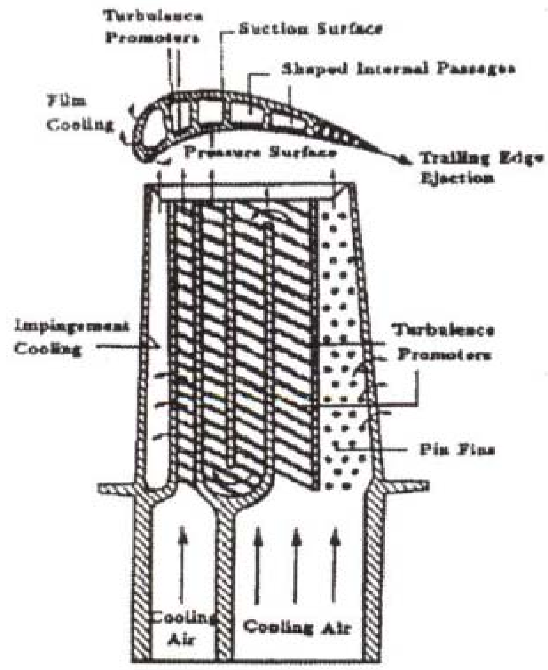

Figure 2. Turbine blade internal cooling passage [from Zhang et al.,1993]

A new innovative technique, which entails implementing an array of staggered pins in a blade shroud and then covering it with a metal layer, was recently introduced. The air after its passage through the micro-exchanger passages can be driven outwards for external film cooling. Two manufacturing attempts have been reviewed; one by electro-chemical deposition (Ref. 3), the other one by LIGA process (Ref. 4).

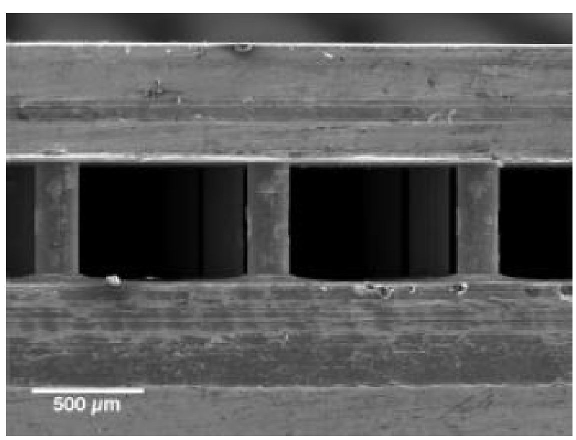

Figure 3. SEM of the heat exchanger [from Marques, 2002]

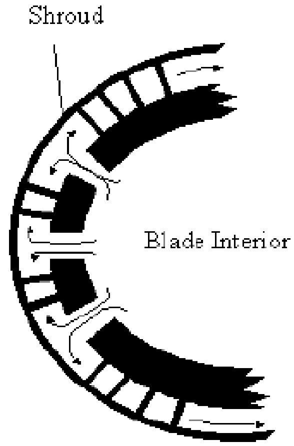

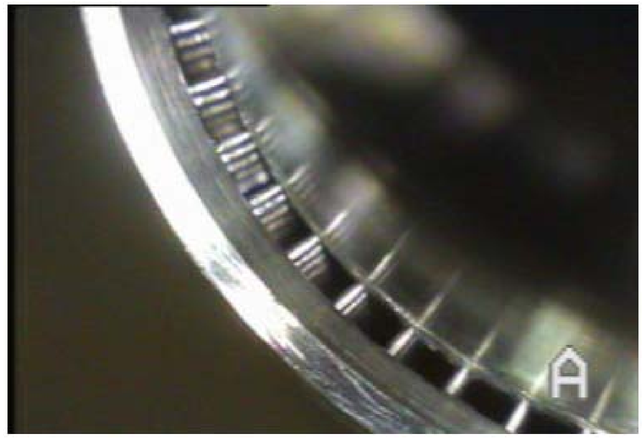

Figure 4. Cross section of heat exchanger in stainless steel tube [from Marques, 2002]

The above figures present the configuration of the exchanger mounted on a model blade and the operation during which air flows through the array and cools the hot blade.

A definition sketch of the chosen micro-heat exchanger array geometry consisting of cylindrical pins is shown in figure 5. In the geometry, X stands for the streamwise pitch between two pins, S is the span-wise pitch, H is the pin length/height and D is the pin diameter. This nomenclature is consistent with the literature.

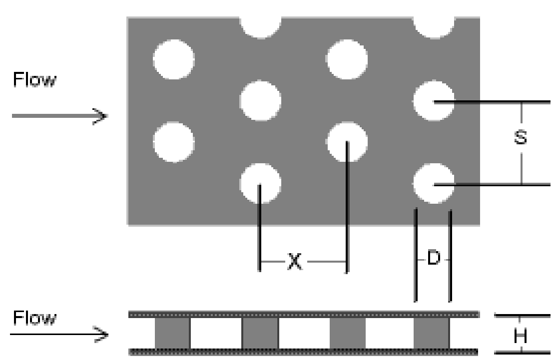

Figure 5. Heat exchanger scheme with the common symbolism [from Choo, 2003]

B. LITERATURE REVIEW

Most of the work in this area so far has been empirical and mainly in the macro-scale. Several researchers tried to understand the performance of different array configurations, in several conditions, by an examination of factors like the Nusselt number, the heat transfer coefficient and the friction factor. The latter is as significant as the other heat transfer characteristics, since in order to evaluate a configuration, the pressure drop has to be considered. The usual goal in these studies is to optimize the array to provide the greatest heat exchange rate with the least expended work for any flow condition.

One of the early contributions came from Van Fossen (Ref. 5), who studied the effect of the presence of pins with different H/D values, for a range of Reynolds number from 3,000 – 60,000. He concluded that the presence of the array returned higher heat transfer coefficient values compared to an empty duct and they got higher as the H/D was increased. His results correlated better flows over a Reynolds number of 6,000.

Metzger et al. (Ref. 1, 6) developed accurate correlations for configurations in which the stream-wise distance ratio was varied while the others were kept constant. Those correlations for the Nusselt number were validated by Hamilton (Ref. 7) with a numerical model. Also Metzger was one of the few who tried to examine the effects of using other types of pins, like oblong shaped, which was also the research subject of Arora (Ref. 8). Both Metzger and Arora concluded that the friction factor was significantly lower, but the heat transfer rates did not approach the cylindrical pin values.

Chen et al. (Ref. 9) later examined more aerodynamically shaped pins like tear drop shaped fins. They concluded that these pins offer higher performances, and better heat transfer rates, with almost half the friction factor of the round pins. Those findings were corroborated by Hamilton, who found that the optimum airfoil shaped pin array outperforms a similar cylindrical pin array, which needs triple the specific energy loss to produce analogous heat transfer rates.

There has been considerable deliberation among the researchers with regard to the heat fluxes from the pins compared to the endwalls. Chyu et al. (Ref. 10) show comparable fluxes between these two parts of the exchanger; unlike Metzger and Van Fossen, who showed that the pins generated 50 percent higher heat transfer rates than the end-walls. On the other hand, Al Dabagh et al. (Ref. 11), found that end-walls show heat transfer rates 35 percent higher than the staggered pins. Finally, Chyu et al. (Ref. 12) in alter study found that the pin surfaces offer around 20 percent more in heat transfer than the endwalls. Furthermore their results for the Nusselt number are very close to those reported by Metzger (Ref. 6)

Also very interesting is the approach of Tahat et al. (Ref. 13, 14), who tried to correlate the Nusselt number with the Reynolds number, including the geometry configuration of the tested arrays by using the ratios of the stream and the span-wise distance of the pins over the total length and width of the array. They used a specific test bed with a varying ceiling height to test different pin bank arrangements to find the optimum spacing for the pins.

In 1997, Li et al. (Ref. 15) conducted an experimental work with elliptical pin arrays and compared their data with Metzger's findings. They used the same dimension pins in two different arrays, but with equal stream and span-wise distance between them, for a range of the Reynolds number 800 – 9,000. They found better heat transfer rates with considerable lower pressure losses. The more packed his configuration was, the greater the performance with resulting higher Nusselt numbers.

One of the most recent, and probably the first in micro dimensions experimental work is by Marques et al (Ref. 16), who tested the configuration of X/D=S/D=2.5 and H/D=1 for Reynolds number from 4,500 to 19,200. The same configuration was also tested by Metzger and Chyu in the past, but in the macro-scale. Marques et al. developed a correlation for the Nusselt number for the range of Reynolds noted above, which gives more optimistic results than the other two researchers. A possible explanation is that their theoretical model uses a smaller heat exchange area in the array than the exchanger footprint area. They then developed a theoretical model that can compute the performance of such a heat exchanger when it is used under a shroud in a turbine blade to cooling it.

Finally, at the Naval Postgraduate School, Monterey, California, in 2002-04 an experimental apparatus was built for testing a set of compact heat exchangers by Roussakies (Ref. 17) and Bosserman (Ref. 18). The arrays are the same as those that will be studied in this work. Because some design issues of the testing bed facility arose, the results are not as reliable as had been expected which a good reason for also checking them against a numerical model.

On the other hand, little numerical modeling work had been done until recently in comparison with empirical. Recent advances in CFD tools have made this a very promising avenue of research. Two important factors in the push toward that direction are the great manufacturing and testing difficulties and the high cost that these studies demand.

Donahoo et al. (Ref. 19) developed a two dimensional model of staggered pin arrays, by using a general purpose viscous solver, in order to optimize their configurations in axial pitch (X/D) spacing for turbulent Reynolds numbers. They found that the maximum heat transfer occurred between the fourth and sixth row for the tested arrays. Finally they recognized that a 3 D model is a future necessity since it was not possible to capture the pin–endwall interactions with the 2 D model and compare their participation to the whole heat transfer of the array or to study the effect of the H/D ratio.

Hamilton (Ref. 7) used the finite element commercial code "ANSYS" to develop a numerical 3 D model to study several configurations of staggered pin-fin heat exchangers, but still in the macro-scale. Initially, he validated his model with prior experimental results from Arora et al. and Metzger et al. He then proceeded to examine of the performance of arrays with cylindrical pins. He developed correlations for the Nusselt number for all his configurations, and also found that pin surfaces had from 50-200 percent higher heat transfer coefficients than the walls. Achieving small increases of it requires disproportional increases in friction power losses. He concluded that variations in axial pitch did not have as great an effect in performance as those the in H/D ratio. He also studied airfoil-shaped pin arrays, from which he concluded that they are better performers than corresponding dimensional cylindrical pin arrays since, to attain comparable heat flux removal, they require only a third of the energy as compared to the latter.

Choo (Ref. 20) carried out a laminar flow numerical analysis in 2003. He simulated exchangers performing in micro-scale in the laminar regime with Reynolds numbers in the range of 100-1,000 to study the effect of the geometrical ratios of the exchangers (X/D, S/D, H/D). He stated that for his geometries and simulations the maximum heat transfer occurred around the second row of the models. Also, after taking into account all three effects, he suggested that the optimum configuration of his matrix was X/D=1.25 and S/D=H/D=3.

To minimize the amount of time and cost that are needed in an empirical project, use of a computational study for pre-evaluation and optimization of several designs is absolutely essential. Another characteristic worth mentioning is the tremendous flexibility that a computational study can offer as compared to empirical methods. Finally, the attributes of the theory that were developed for the macro-scale studies can also be directly applied to micro-scale, since they are based on the same characteristic qualitative factors.

C. OBJECTIVES

The main objective of this study is to determine the performance and characteristics of flow and heat transfer behavior of a set of micro heat exchangers of specific configurations. A 3-D model will be developed that will be validated by theoretical and historical experimental results in order to use it to examine the behavior of the different staggered cylindrical pin arrays in a laminar compressible flow regime.

The parameters that will be inspected are the Nusselt number, the heat transfer coefficient, the Mach number, the array pressure drop, the friction factor, and the specific fluid friction power for different Reynolds numbers .The theoretical definitions for the above parameters will be provided in the following chapter. The results will be used to define suitable regions-conditions of operation for every heat exchanger's geometry and will be compared to findings of experimental tests already completed.

D. METHOLOGY-ORGANIZATION

Several three-dimensional models were constructed according to our test matrix, using the commercial, computational fluid dynamics package CFD-ACE+. The construction was carried out with the preprocessor of the package CFD-GEOM. Then the models were transferred to the processor CFD-ACEU for executing the simulation. Finally, the postprocessor of the package CFD-VIEW was used to study, analyze, and manipulate the results. The details of the modeling will be discussed in the next chapter. In the third chapter we provided the validation and corroboration with the theoretical and historical results and a more extensive heat exchange examination of the observations. In the fourth chapter the results of the simulations of the tested configurations are discussed. The final chapter draws certain conclusions and provides some recommendations.

THIS PAGE INTENTIONALLY LEFT BLANK

II. FINITE VOLUME MODELING

A. MODELING GENERAL DESCRIPTION

The CFD-ACE+ package solver was used in this study. It is a solver that uses a finite volume pressure correction based method to solve the conservation equations of mass, momentum and energy. The software provides the user with three graphical user interfaces (GUIs): GEOM for the geometries-models creation, the ACEU that is the actual solver of the discretized equations, and the postprocessor VIEW for viewing and post-processing the results. CFD-ACE+ has been very popular for this kind of problem, such as fluid flow fields in conjugation with heat transfer, because it provides reliable results for a variety of problems. This independence makes this solver more powerful since it provides very similar results for several grid refinements within good accuracy.

B. TEST MATRIX

The test matrix of this study consists of ten different configurations. The first eight configurations and the tenth have been tested here at the Naval Postgraduate School by testing Bosserman and Roussakies; but because of some construction constraints and limitations of the utilized bed, their data is still preliminary and is being verified. All of the configurations have the same height due to the specific height of the flow channel inside the designed apparatus (H=405μm). The first four have a pin diameter of 500μm (D=500μm), while the next set of four has a pin diameter of 166.7μm (D=166.7μm). The tenth one has a pin diameter of 151.5μm; it was Summers (Ref. 21) optimum laminar configuration in the macro-scale level. The two sets of four vary under the same ratios for the stream-wise and the span-wise pin spacing. This can be observed in the following table, which presents the tested matrix, with some geometric characteristics that will be explained thoroughly later in this chapter.

Table 1. Test matrix for the heat exchanger configurations

#	X/D	S/D	H/D	D (μm)	αH	D_h(μm)	$V_{open}(m^3)$	$A_{wetted}(m^2)$
HX#1	3	3	0.81	500	2.11	701	8.32E-10	4.74E-06
HX#2	1.25	3	0.81	500	2.26	567	3.00E-10	2.12E-06
HX#3	1.25	1.25	0.81	500	2.62	307	7.87E-11	1.02E-06
HX#4	3	1.25	0.81	500	2.26	567	3.00E-10	2.12E-06
HX#5	3	3	2.43	167	2.67	553	9.24E-11	6.68E-07
HX#6	1.25	3	2.43	167	3.62	354	3.34E-11	3.77E-07
HX#7	1.25	1.25	2.43	167	5.88	137	8.74E-12	2.55E-07
HX#8	3	1.25	2.43	167	3.62	354	3.34E-11	3.77E-07
HX#9	2.5	2.5	1	500	2.25	777	6.83E-10	3.52E-06
HX#10	5	5	2.67	152	2.27	690	2.25E-10	1.30E-06

The ninth configuration is the one used most by the researchers, especially in the macro-scale and it is the one that is going to be used for validations and corroborations, along with the seventh, which has the largest magnification factor (αH) and is the “densest” of all of them. The area density of an array unit cell is defined as the ratio of the wetted (heat transfer) surface area over the total volume. The magnification factor that is provided in the table is defined as the product of the area density and the pin height. For an exchanger without pins that is a rectangular cross sectional duct, the αH becomes equal to 2. All the above table values have been computed based on a unit cell.

Table 2. Unit cell dimensions for the tested heat exchangers

#	X/D	S/D	H/D	D (μm)	S (μm)	X (μm)	H(μm)
HX#1	3	3	0.81	500	1500	1500	405
HX#2	1.25	3	0.81	500	1500	625	405
HX#3	1.25	1.25	0.81	500	625	625	405
HX#4	3	1.25	0.81	500	625	1500	405
HX#5	3	3	2.43	167	500	500	405

HX#6	1.25	3	2.43	167	500	208	405
HX#7	1.25	1.25	2.43	167	208	208	405
HX#8	3	1.25	2.43	167	208	500	405
HX#9	2.5	2.5	1	500	1250	1250	500
HX#10	5	5	2.67	152	758	758	405

The dimensions of the unit cells for all the configurations are shown in the Table 2. The heat exchangers have been divided into two groups and they will be examined according to their pin diameter.

C. BOUNDARY CONDITIONS

Several assumptions had to be made for the purpose of reducing the computational requirements. Because the geometry and scale of the micro heat exchanger it usually contains a large number of pins, and the contribution of pins as compared to the endwalls in heat transfer will be sufficiently greater. Micro heat exchangers have a very large number of pins in the span-wise direction, and the contribution of the side walls in the heat exchange process could be relatively neglected. Instead Hamilton found that it is sufficient to consider only 2 spanwise rows and introduce symmetry sidewall boundary conditions to account for the ignored rows. A symmetric boundary was also assumed at the Hx midplane in order to simulate only half of the geometry. The symmetric planes have the zero cross-over velocity components, and from the thermal perspective is are adiabatic in nature. Furthermore, the wall boundary condition was used for the pin surfaces and the lower endwall where the no slip condition was applied.

From the heat transfer point of view, the pins and the lower endwall were assumed to be isothermal. A justification calculation for the isothermal character of the pins can be found in Hamilton (Ref. 7). An illustration of the model is presented in figure 6.

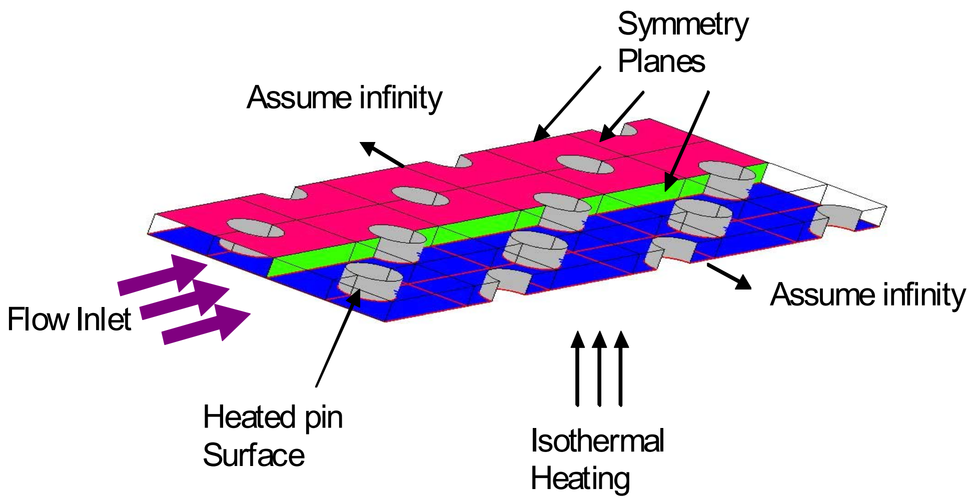

Figure 6. Schematic of the numerical model

To validate the models with the theoretical and historical experimental results, an entry and an exit straight duct section was used. The entry duct is used to provide a fully developed velocity profile at the flow entrance to the exchanger; while the exit duct will provide well mixed conditions for the flow so as to make the exit temperature calculations more effective and robust. Subsequently, we used the concept of the entry and exit ducts in all the array configurations in order to be consistent. In both ducts we applied the same boundary conditions for the surrounding planes. The sidewalls and the upper plane were assumed to be adiabatic symmetry planes, while the bottom was assumed to be an adiabatic wall. Furthermore, we assumed an inlet with a fixed velocity that fixes the mass flow rate and thus the Reynolds number of the simulation and a fixed pressure outlet boundary. A representation of the above conditions is provided in the figure 7.

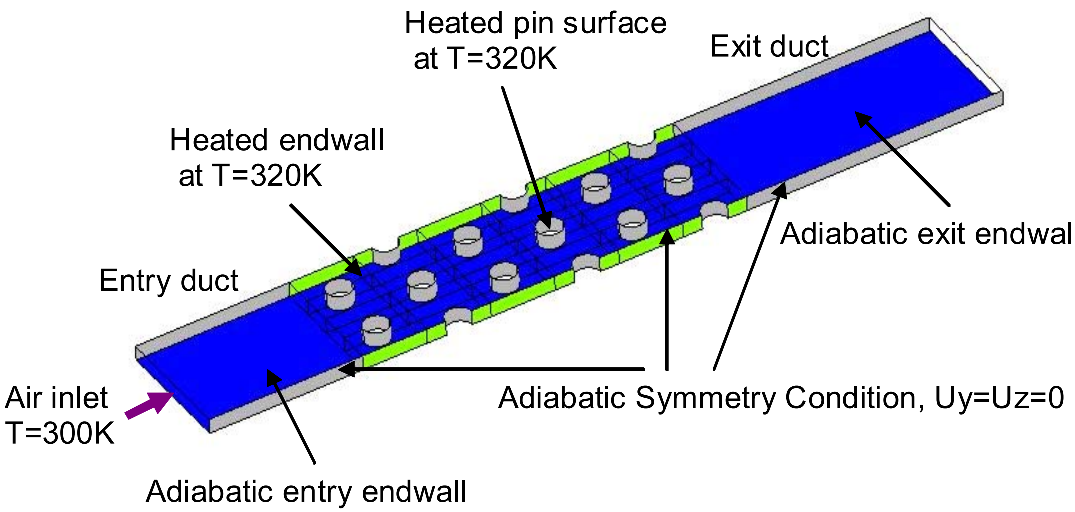

Figure 7. Boundary conditions representation

D. GRID GENERATION

Since we decided to use the "GUI" of the GEOM and not the PYTHON scripting feature, we had to create several geometrical models independently. First, the 2-D model of a half unit cell had to be constructed, since we intended to use an unstructured triangular meshing. Thus the creation of a closed loop was unavoidable. The next step was to duplicate that half unit cell at the proper position, according to every array configuration. We did a very careful meshing that was finer near the pin's perimeter and coarser towards the internal part, to capture the large heat and flow gradients near the walls. In most cases we used a 30 degrees curvature criterion and a growing factor from 1.05 to 1.10. Then we linearly extruded the whole geometry toward the third direction by using a power law with the purpose again to create layers of triangular prisms that will be finer near the heated endwall where the gradients are also expected to be higher. We carefully examined all the 3-D centroid / face angles to ensure that were at least

25 degrees and also that no negative volume cells had been created. Figure 8 provides a fingerprint illustration of the grid around a unit cell of an array.

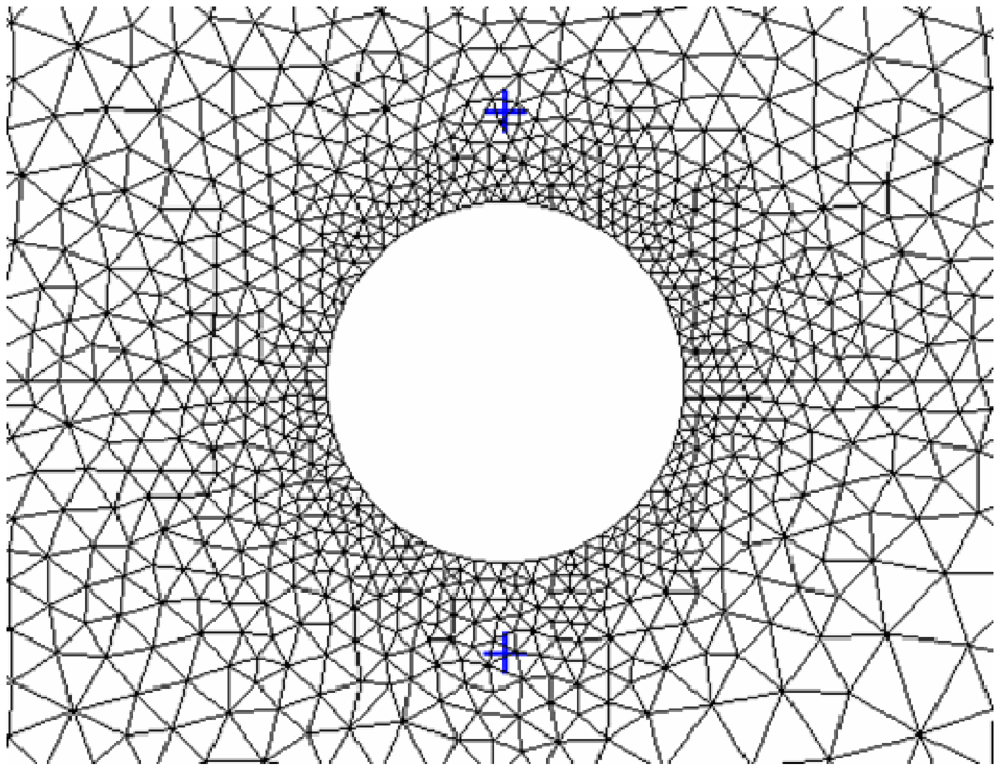

Figure 8. Sample unit cell's meshing in 2-D

Another issue was the entry length in the ducts. Since we had to construct several configurations and run them in different Reynolds numbers we had to figure out a way to reduce the model generation work and eliminate the need for different ducts for every simulation. This was achieved by using a feature of the solver ACE where we can simply input the velocity profile for the inlet boundary to ensure fully developed conditions. Therefore, we used a constant length duct for all the models that were generated, with lengths of three and five hydraulic diameters for the entry and exit sections respectively. Since the height of all the models is the same, the duct hydraulic diameter for all the models is constant and equal to twice the height for an infinite span-wise model.

Because we used structured grids for meshing the two ducts, the whole model had a hybrid character, and we tried not to exceed a block aspect ratio of five in the cell extrusion process. This would serve the connection regions between the two grids for having similar cell dimensions to ensure a smooth transition from one volume to the next.

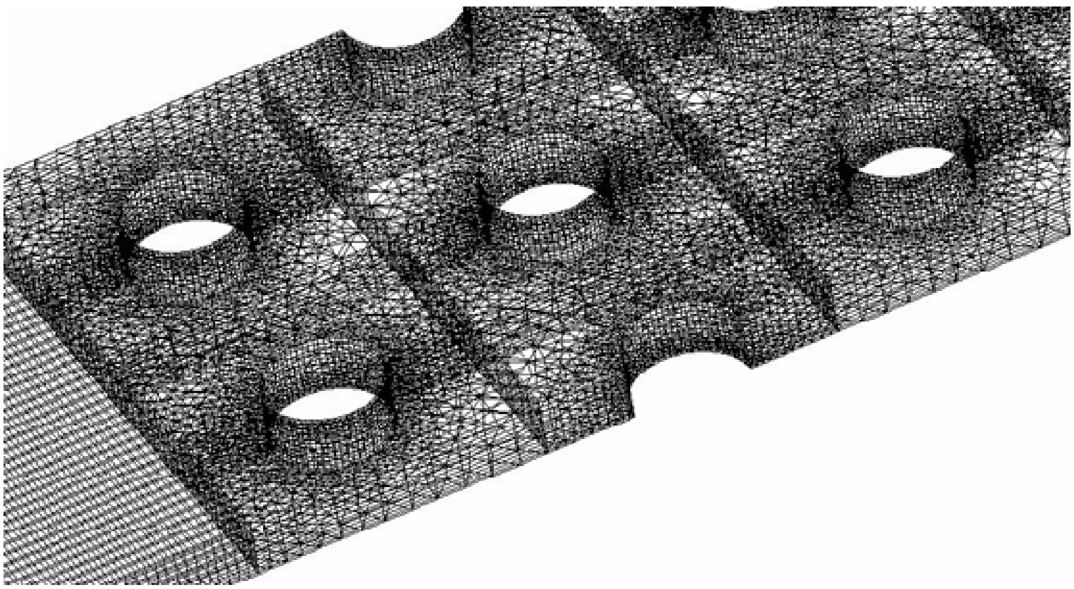

Figure 9. Sample model's grid

Figure 8 illustrates a sample mesh of a model. After the generation of any geometry we had to scale it in micrometers in order to import that into the solver GUI.

E. SOLUTION METHOD – SOLVER CONTROLS

As mentioned previously the simulations were executed in the laminar regime. Hamilton (Ref. 7) in his dissertation showed that the transition typically occurs at a Reynolds number 1000-1500. Within that region, he achieved an overlap in a figure of the laminar and turbulent models that he used. Zhukauskas (Ref. 23) makes a similar statement in his research review. The Reynolds number on which our runs are based extended from 100 to 1,000.

In the CFD–ACE+ solver the flow and heat transfer modules were selected in order to obtain the flow (velocity and pressure) and temperature distributions for the fluid volume elements. To formulate an equation for the unknown variable pressure, the continuity equation is solved by adopting the SIMPLEC algorithm in CFD – ACE to start the iteration process. For more information, the reader is referred to the user manual (Ref. 24) or the book by Versteeg and Malalasekera (Ref. 25).

In regard to the volume conditions, because we are going to solve the compressible form of the numerical models, the density is defined from the ideal gas law, which is the sixth equation in the governing equation set. Furthermore, the air viscosity was obtained by using Sutherland's law for. Also, the air pressure coefficient C_p was held constant, since its variation in the region of 300 – 320 K is negligible. For the thermal conductivity, which varies more than the pressure coefficient, we used the constant Prandtl number law which is a variation of k according to the definition of the Prandtl number which is held constant at a value of 0.707.

$$Pr = \frac{C_p * \mu}{k} \Rightarrow k = \frac{C_p * \mu}{Pr} \quad (1)$$

The next step in the solver tabs is to input the boundary conditions. The velocities for the wall boundaries, pins and endwall were kept at zero and the temperature was set to 320 K. The inlet temperature was set to 300 K, and for the flow part we input a fully developed X-velocity profile in the Z direction. The profile for every Reynolds number and for every array was calculated by using an ECXEL spreadsheet; which was then utilized by the solver to fix the mass flow rate which subsequently derives the Reynolds number for this simulation.

For the flow initial conditions we input a velocity that was based on the duct cross sectional area and was derived by dividing the specific mass flow rate with by duct area and film density, while the initial temperature was set to 300 K.

Another crucial control is the scheme that we had to choose in order to discretize the advection term, especially when this term dominates other terms in the governing equations. The monotone streamline upwind (MSU) scheme is generally quite robust and produces stable diagonally dominant matrixes, but is first order accurate. It is also the scheme recommended in the ACE+ manual, especially for complex geometries.

Trial runs were carried out using other second order schemes like the central, or the upwind limiter, always blended with the MSU to prevent divergence. The same scheme is also suggested by the solver manual documentation. We tried to overcome the choice of the first order scheme by increasing the convergence criteria for the residuals average and by using more refined models for the simulation. As an example of the deviation between the schemes for HX#7, and for the case of Re=100, the percentage difference between the upwind and the central, as far as it concerns the heat addition to the fluid was 0.2 percent and between the upwind limiter was 0.3 percent.

As far as it concerns the relaxation criteria, in most cases the solver default values worked well, except for the higher Reynolds number simulations, near 1,000, where we had to modify them a little by increasing the inertial relaxation values up to 0.3 - 0.4 and by decreasing the linear ones down to 0.9 in order to provide more stability to the solution. This slowed down the convergence process but made it achievable.

F. NUMBER OF PIN ROWS

Another issue that we had to resolve was the number of pin rows that we were going to use for every array that we were going to model. Because of the great variation of the configurations, a great variation in their performances was expected. For every configuration, and especially for the lower Reynolds number simulations, the bulk outlet temperature was expected to be higher. It began to reduce as the Reynolds number was increased, which agrees with the theory, in Kays and Crawford “Convective Heat and Mass Transfer” (Ref. 26). So for every array we had to use only so many rows of pins that would yield an outlet bulk temperature no more than 319 K to 319.5 K, or 0.5 to 1 K lower than the prescribed wall and pins temperature of 320 K, in order to avoid errors due to loss of resolution in the numerical calculations.

Therefore, for every configuration we generated a geometry without ducts and with ten rows of pins, and we ran that for Reynolds of 100. Then by utilizing CFD – VIEW, we constructed a carpet plot of the temperature for the upper symmetry plane, illustrated in figure 10, to get an initial rough estimate in which row we achieved a temperature around 319 K.

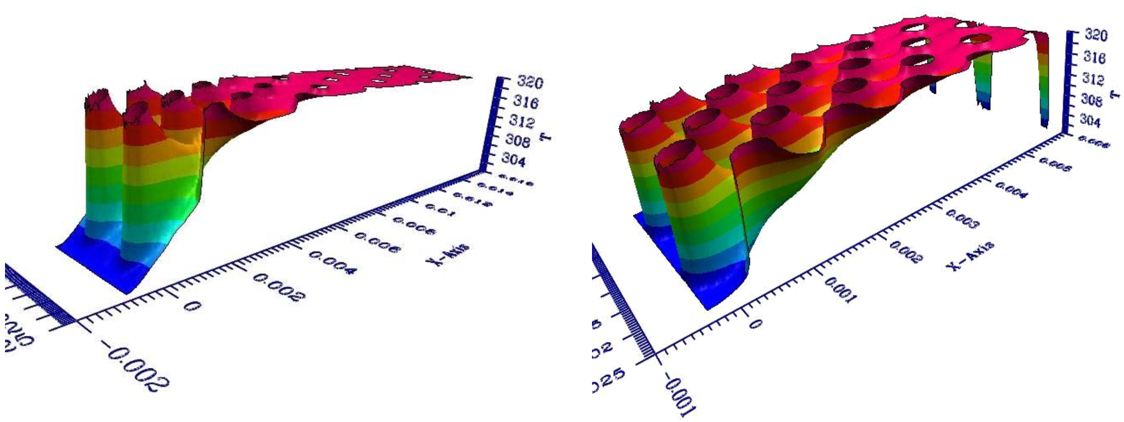

Figure 10. Temperature profile for two pin arrays with ten rows

Then for higher accuracy we went to this row of fluid blocks, made a stream wise direction (X) cut and integrated the results on that plane. This was done, to find an accurate bulk temperature at that exact X coordinate. By moving the cut in the selected row blocks we could check the temperature continuously in every position.

Then we went back to GEOM to generate a final version of the model with the desired number of pin rows and with the entry and exit duct as it were described above for the specific runs.

Table 3. Number of pin rows used per configuration

#	X/D	S/D	H/D	Nx	Ns	L(m)	W(m)
HX#1	3	3	0.81	6	2	0.0090	0.0030
HX#2	1.25	3	0.81	10	2	0.0063	0.0030
HX#3	1.25	1.25	0.81	4	2	0.0025	0.0013
HX#4	3	1.25	0.81	4	2	0.0060	0.0013
HX#5	3	3	2.43	8	2	0.0040	0.0010
HX#6	1.25	3	2.43	10	2	0.0021	0.0010
HX#7	1.25	1.25	2.43	4	2	0.0008	0.0004
HX#8	3	1.25	2.43	4	2	0.0020	0.0004
HX#9	2.5	2.5	1	6	2	0.0075	0.0025
HX#10	5	5	2.67	8	2	0.0061	0.0015

Table 3 provides the specific number of rows that every heat exchanger configuration used. All the simulations used two unit cells in the span-wise direction. In the above table the dimensions of the configurations for all the heat exchangers are also presented.

G. THEORETICAL APPROACH

1. Characteristic Length

The most appropriate characteristic length that is the hydraulic diameter of this Hx array is obtained from flow theory in porous media, and is defined as follows in terms of the open volume that is available for the fluid flow in the array and the wetted heat transfer surface area:

$$D_h = \frac{4 * V_{open}}{A_{wetted}} \quad (2)$$

It is the most truly dimensionless quantity that represents consistently the tortuous flow paths inside the exchanger. It is the same characteristic length that was proposed by Van Fossen (Ref. 5) and that is used by many more recent experimental and numerical researchers. The hydraulic diameter remains the same whether its calculation are made based on the unit cell or based on the whole array.

2. Entry – Exit Length Considerations

According to White (Ref. 22), for every Reynolds number the relation that gives the entrance length for a fully developed flow is the following:

$$L_e \approx 0.06 * D_h * Re_{Dh} \quad (3)$$

Because it was not possible to construct a different entry duct for every simulation and because the existence of ducts usually smoothes the flow conditions, we decided to impose a fully developed velocity profile and to use the constant length specified above for all the flow conditions.

For the exit duct length, which is more crucial because it is necessary for ensuring a well mixed flow that is starting to redevelop again and because it will help in a more accurate integration for computing the predicted outlet bulk temperature, we used a little longer section than the entry one, equal to five hydraulic diameters.

3. Inlet Velocity Considerations

According to White (Ref. 22), the relation that gives the velocity profile for a Poiseuille flow between parallel plates is

$$u = u_{max}(1 - \frac{z^2}{H^2}) \quad (4)$$

where u_{max} is the maximum velocity at the centerline of the duct, which is equal to

$$u_{max} = \frac{3}{2} V_{in} \quad (5)$$

where V_{in} is the average inlet duct velocity. Consequently by using the equation (4) we created a six - point profile along the z-axis, which then was used at the definition of the inlet boundary condition in the solver.

4. Reynolds Number

The Reynolds number that we are going to use is based at the previously defined hydraulic diameter and in a characteristic velocity, the average array velocity

$$Re = \frac{\rho \bar{U} D_h}{\mu} \quad (6)$$

where $$\bar{U} = \frac{\dot{m}}{\rho \bar{A}} \quad (7)$$

and $\bar{A}$ is the average array cross sectional area, which is equal to

$$\bar{A} = \frac{V_{open}}{L} \quad (8)$$

Also, according to the above relations, the Reynolds number can be expressed associated to the mass flow rate. This relation will be used after every simulation to calculate the exact Reynolds number from the "mass flow summary" from the output file of ACE.

$$Re = \frac{\dot{m} D_h}{\mu \bar{A}} \quad (9)$$

H. COMPARED PARAMETERS ANALYSIS

1. Nusselt Number

The Nusselt number is a dimensionless number that provides the ratio of the convective heat transfer over a surface that would occur by fluid motion to the corresponding conductive heat transfer and is a measure of the heat transfer ability. In our case more meaning makes the average Nusselt number which is given by the following relation:

$$Nu = \frac{\bar{h}_{array} D_h}{k} \quad (10)$$

where $\bar{h}_{array}$ is the average array heat transfer coefficient and can be calculated by using the thermal energy difference between the flow inlet and the outlet, which is provided by the heat transfer summary in the output file of ACE at the end of the simulation, and by using the log mean temperature difference as below:

$$\bar{h}_{array} = \frac{\Delta Q}{A_{wetted}\Delta T_{lm}} \quad (11)$$

For computing the log mean temperature difference we will use the definition of the outlet bulk fluid temperature, which, according to Kays and Crawford in "Convective Heat and Mass Transfer" (Ref. 26) is provided from

$$\dot{m}T_{bulk,out} = \int_{A_c} u\rho T_{out} dA_c \Rightarrow T_{bulk,out} = \frac{\int_{A_c} u\rho T_{out} dA_c}{\int_{A_c} u\rho dA_c} \quad (12)$$

In the above definition the Cp is not included because we had assumed already that it is constant and does not influence the relation. The outlet bulk fluid temperature was calculated in the VIEW program by integrating at the outlet of the adiabatic exit duct with respect to the duct cross sectional area by using the expression calculator feature. It is the temperature that characterizes the average thermal energy of the flow, since it is based at the mass flow rate.

The log mean temperature difference is given by the formula below;

$$\Delta T_{lm} = \frac{(T_{wall} - T_{bulk,in}) - (T_{wall} - T_{bulk,out})}{\ln\left(\frac{T_{wall} - T_{bulk,in}}{T_{wall} - T_{bulk,out}}\right)} \quad (13)$$

where the inlet bulk fluid temperature was constant and equal to 300K.

2. Effective Heat Transfer Coefficient

The effective heat transfer coefficient is the corresponding heat transfer coefficient in an empty (without pins) open channel had to provide in order to transfer the same amount of thermal energy like the one with the pins.

$$\bar{h}_{eff} = \bar{h}_{array} \frac{\alpha H}{2} \quad (14)$$

It is an average quantity of the whole array since it is based at the average array heat transfer coefficient, and it becomes equal to it for the open channel because $\alpha H=2$.

3. Friction Factor

The dimensionless friction factor of the pin array that was used was defined as follows:

$$f = \frac{\Delta P_{array} D_h}{\frac{1}{2}\rho \bar{U}^2 L} \quad (15)$$

where ΔP_{array} was the total pressure difference between the inlet and outlet sections of the array. It was computed from the VIEW post processor by integrating at the sections with the expression calculator tool in order to find an average value of the inlet and outlet section. L is the total stream-wise length of the array. Also, the density that was used was the one based on the standard atmospheric conditions but calculated in the film temperature, in order to have the same measure of comparison between the different heat exchanger configurations.

4. Specific Fluid Friction Power

Kays and London (Ref. 27) define a quantity that can express the performance of a heat exchanger, the specific fluid friction power, which characterizes the work that must be expended to overcome the viscous effects per unit wetted area.

$$E = \frac{\dot{m}\Delta P_{array}}{\rho_{film} A_{wetted}} \quad (16)$$

5. Effectiveness - NTU Relations

According to Incropera and De Witt in "Introduction to Heat Transfer" (Ref. 28) the effectiveness of a heat exchanger is defined as the ratio of the actual heat transfer rate to the maximum possible heat transfer rate and, in our case, is defined as:

$$\varepsilon = \frac{T_{bulk,out} - T_{bulk,in}}{T_{wall} - T_{bulk,in}} \quad (17)$$

The same source shows that, for all the exchangers, the effectiveness associated with the number of transfer units (NTU) is given by the following relation:

$$\varepsilon = 1 - \exp(-NTU) \quad (18)$$

The NTU generally is defined as

$$NTU = \frac{UA}{C_{min}} \quad (19)$$

but in our case as

$$\frac{1}{UA} = \frac{1}{\bar{h}_{array} A_{wetted}} \quad (20) \quad \text{and} \quad C_{min} = \dot{m} C_p \quad (21)$$

6. Maximum Mach Number

The maximum Mach number was extracted with the post processor by examining the fluid volume inside the array and by again using the expression calculator and the max built in function. In order to define suitable operating regions for all the exchangers, the maximum Mach number will be plotted versus the corresponding Reynolds number for comparison.

III. VALIDATION – CORABORATION AND TRANSITION EXAMINATION

A. GRID INDEPENDENCE STUDY

It was anticipated that the simulations of these micro-scale heat exchangers would yield greater performance values when compared to their macro-scale counterparts. This meant that much higher gradients of the concerning parameters were expected to exist within the solutions. Therefore, the need for a suitable grid arose, and this need determined how fine the grid should be. It was a significant effort to obtain valid (grid independent) results. The following section indicates the procedures taken to achieve grid-independent results.

Two prismatic elements were considered for the internal part of the exchangers: a quadrilateral element and a triangular element. Following the element selection, a specific measure was identified to properly quantify the quality of such grids. The most suitable measure for this task was the pin perimeter discretization. Furthermore, to make a consistent grid comparison, the grid growing factors toward the planar and orthogonal directions to the pins' cross sectional area were kept constant. Analogous refinement was also conducted within the entry and exit sections of the heat exchangers.

The grid independent study was performed with the X/D=1.5, S/D=1.5 and H/D=1 heat exchanger configuration with a pin diameter of 100μm. This configuration was selected due to its high area amplification factor, which indicates a very high pin density. It was anticipated that the solutions would have high gradients in all concerning parameters, which gives the solution a very strong dependence on grid refinement. Thus, to achieve grid independence the computed heat transfer flux had to reach less than two percent variation between subsequent grid refinements.

Table 4. Grid independence for model with triangular elements

Parameter	Grid 1	Grid 2	Grid 3
Perimeter division	50	70	90
# of cells	88143	141076	201165
# of nodes	137380	159516	234304
ΔQ (W)	0.00271	0.0027	0.00268
Error (%) for ΔQ	1.12	0.37	0.00
T bulk out (K)	305.49	305.46	305.44

Table 5. Grid independence for model with quadrilateral elements

Parameter	Grid 1	Grid 2	Grid 3	Grid 4
Perimeter division	50	70	90	110
# of cells	87450	139802	198660	278018
# of nodes	72030	118800	172284	245504
ΔQ (W)	0.00257	0.0026	0.00265	0.00268
Error (%) for ΔQ	4.10	2.24	1.12	0.00
T bulk out (K)	305.21	305.32	305.37	305.43

Tables 4 and 5 show the pin perimeter discretization characteristics and the significant data extracted from the simulations. The triangular elements were selected because they proved to be more robust and because the solutions with the triangular elements required less grid refinement to obtain stable outlet bulk temperatures.

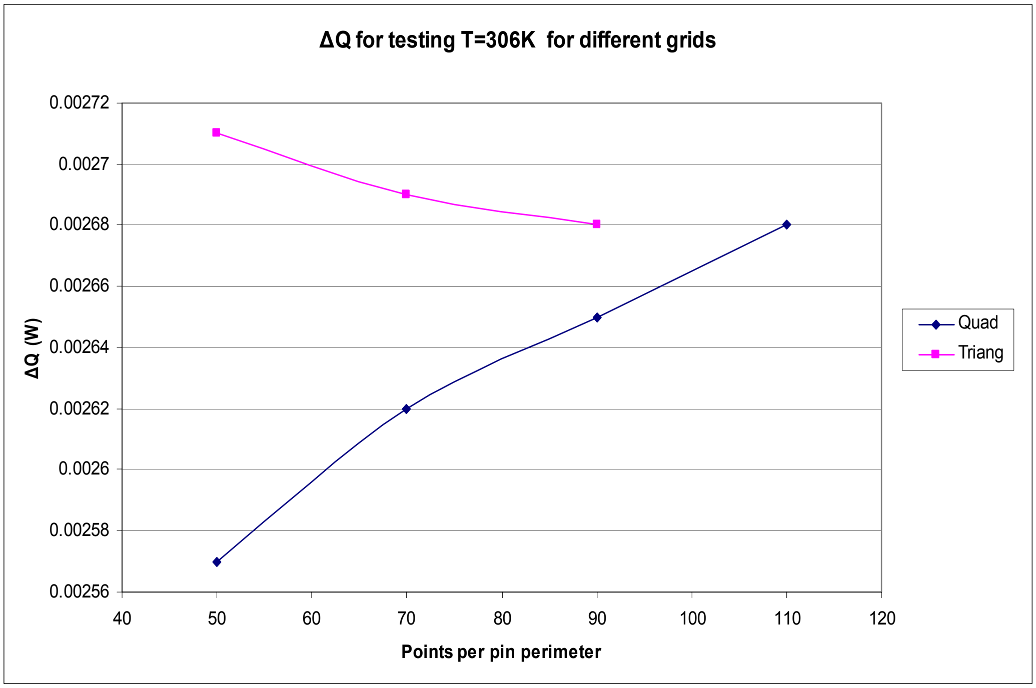

Figure 11. Comparison of heat transfer vs grid quality for the examined models

Figure 11 compares the results from simulations performed with both, the triangular and the quadrilateral element models versus their grid quality (number of discretization points within one pin perimenter.) These tests were performed for the case of Reynolds number of 100. As shown, both models converged to the same solution of 0.00268 W. However, the triangular modeling show results that overestimates the heat transfer when using a grid too coarse to properly capture the high gradients. In contrast, the quadrilateral elements underestimate the heat transfer. Therefore, selecting the triangular elements was simple, specially noting that grid independent results were obtained with 20% less discretization points around the pin perimenter. Furthermore, the deviation from the grid independent result was 300% larger with the quadrilateral elements.

Figure 12, plots the models' performance versus the time required for the simulation execution. Selecting the number of divisions per pin perimeter was also important. From both plots (figures 11 and 12,) the choice of 70 points provided the best trade-off between computational time and accuracy of the results. At 70 points per pin diameter, the results predicted a heat transfer rate of only 0.4% different than the finest configuration (using 110 points).

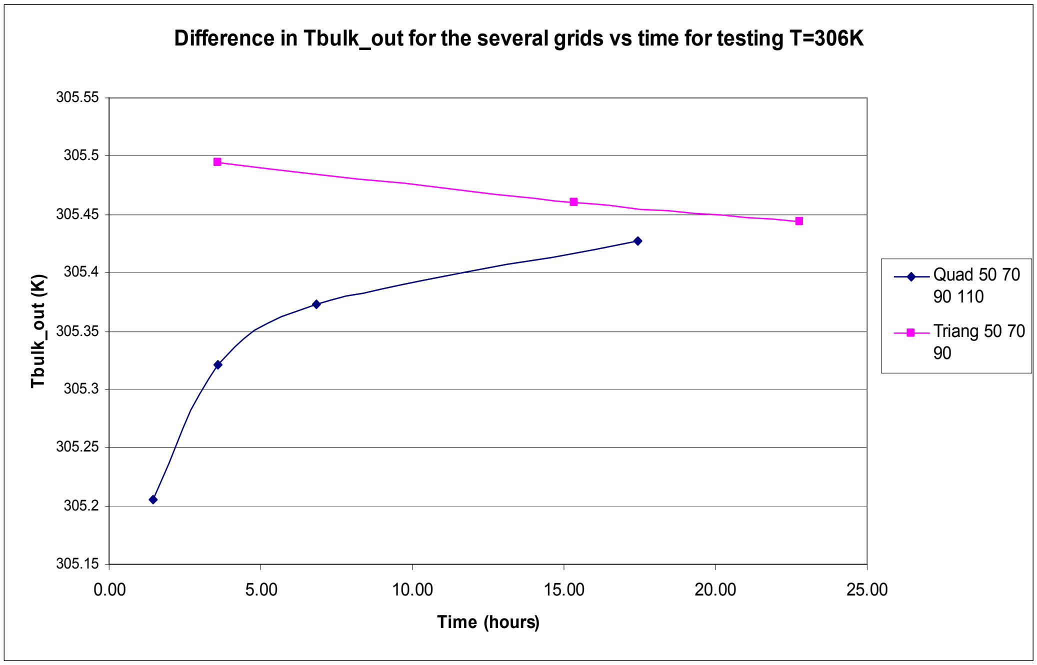

Figure 12. Comparison of the outlet temperature achieved vs. computational time

B. THEORETICAL VALIDATIONS

Numerous inspections were performed in order to validate the results generated by CFD – ACE. The contour plots of temperature, velocity and pressure were examined carefully to verify that they satisfy the boundary conditions. The velocity profiles were inspected for a fully developed condition before the entrance into the array. In addition, the output file generated upon completion of every simulation was carefully examined and analyzed. For example, the mass flow rate computations were examined for an exact agreement with the inlet and outlet boundaries. This was verified by assuring that the imbalance was smaller than 1% of the total value. The heat transfer summary was also carefully inspected. The energy flow into and out of the model at the corresponding boundaries was examined to be equal to the total amount added from the pins and the endwall. Also, the heat imbalance was examined to check if it was an order of magnitude smaller than the net energy addition. However, because the magnitude of the non-dimensional parameters is extremely small (due to the heat exchangers' dimensions,) computation errors were introduced.

1. Energy Balance

This was examined for agreement between the bulk outlet temperature during the post-processing of the results and the temperature that was computed from a simple energy balance according to the following relation:

$$T_{out} = T_{in} + \frac{\Delta Q}{\dot{m}C_p} \quad (22)$$

The ΔQ was computed from the heat transfer summary from the output file runoff each simulation. If the two temperatures had more than a 0.1% difference, the simulation was repeated with a finer grid or with an increased number of iterations. In most cases, we did not have any difficulty, except for a few simulations at a Reynolds number of 1,000 and for some of the configurations with the highest area magnification factors.

2. Effectiveness

The independence of heat exchanger effectiveness was tested by varying the prescribed boundary temperature conditions. Thus, during the grid independence tests, three different boundary temperatures, 306 K, 310 K, and 315 K were used with all the grid refinements. The results, shown in table 6, were extremely close with values within 0.1% from each other.

Table 6. Effectiveness independence of boundaries' temperatures

Model	$T_{wall,1}$=306	$T_{wall,2}$=310	$T_{wall,3}$=315
1st (50 points)	0.868	0.868	0.869
2nd (70 points)	0.887	0.887	0.888
3rd (90 points)	0.896	0.897	0.897
4th (110 points)	0.905	0.905	0.905

For grater assurance, heat exchanger No. 7 was used using two very distinct boundary temperatures, 306 K and 400 K. The effectiveness results were again within 0.1% of each other.

3. Effectiveness Based on NTU

Effectiveness is associated to the number of transfer units (as shown in equation 18). Since this relation is valid for every heat exchanger, it can be used to further validate the computational results. In order to thoroughly test the computational model against the trend of this relation, heat exchanger No. 7 was used. Two different models were created, one with two rows of pins and the second with four rows of pins.. The computed NTU results are plotted in the purple squares of figure 13.

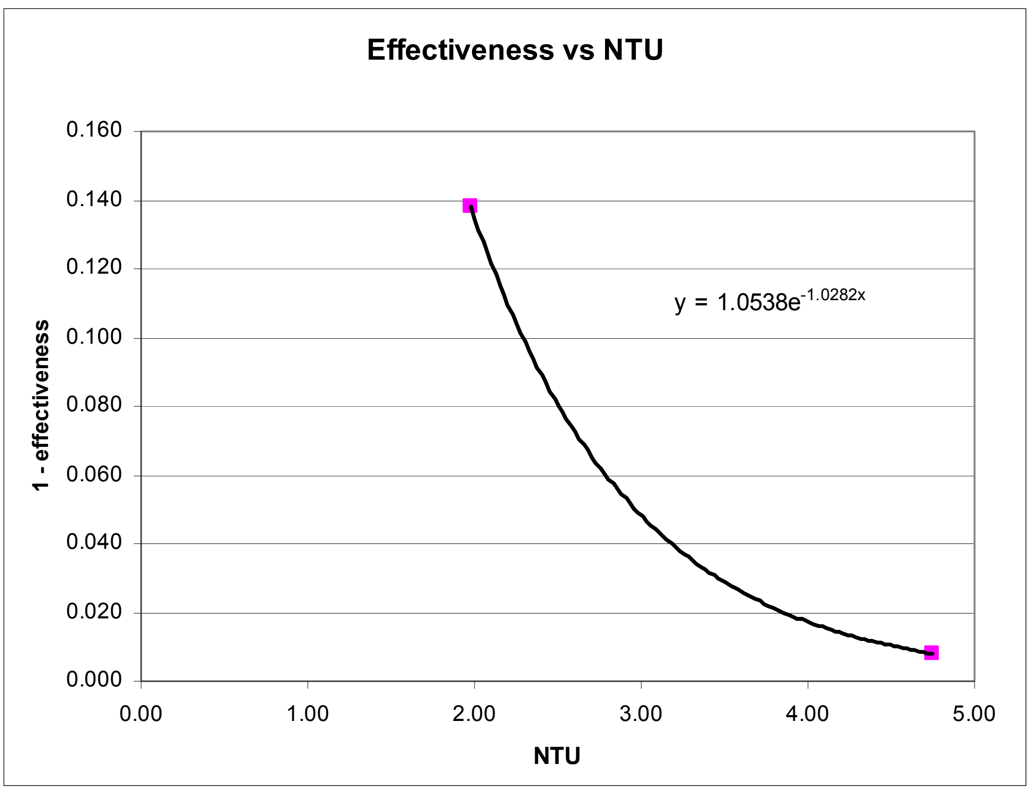

Figure 13. Effectiveness based on NTU for HX#7

The black line in Fig. 13 plots the computed NTU values using Eq. 18, the results show how close the CFD models approach the theory.

4. Compressibility Effects

Our initial ideas of simulating the problem by using a constant density for the models, similar to previous numerical works, collapsed very early since some of the pin-fin arrays are highly packed. It was anticipated that these arrays would require high differential pressures across the array, which breaks down the assumption of constant density.

Heat exchanger configuration No. 7 was used to simulate various mass flow rates with and without variable density configurations. The tests were performed at Re = 100 and 1,000. The variable density model used the ideal gas law to compute the appropriate density values. Figure 14 shows these results, which show significant difference in their friction factors, up to 50% difference at Re = 1,000.

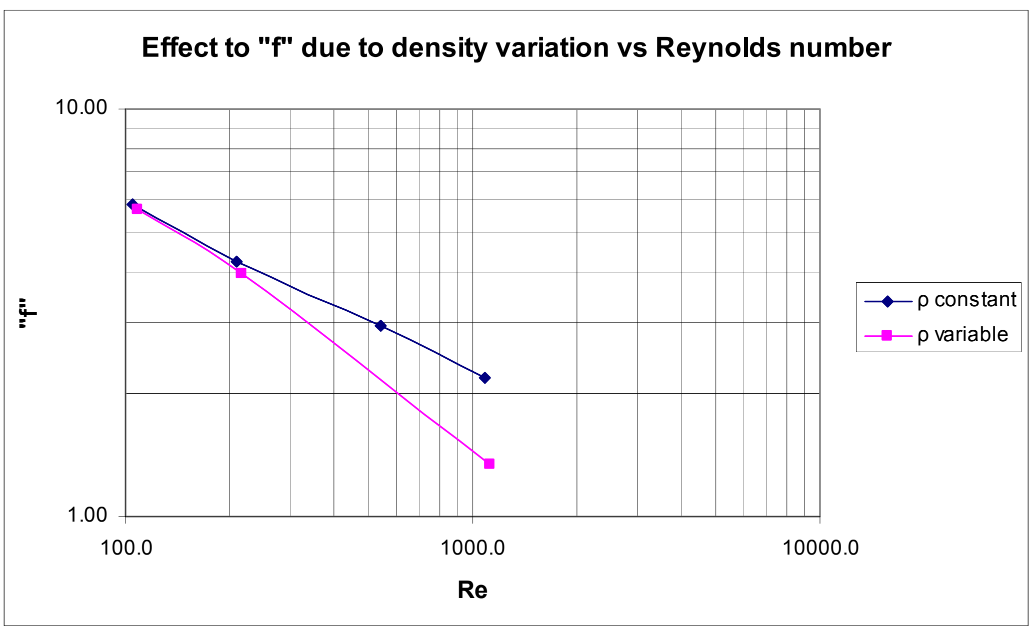

Figure 14. Comparison between constant and variable density for HX#7

Consequentially, variable density was incorporated in all subsequent tests.

C. LAMINAR TO TURBULENT TRANSITION

An examination of the transition region for the micro heat exchangers was also necessary. For this case, heat exchanger configuration No.9 was used, because the results can be corroborated with existing experimental data.

1. Turbulence Modeling

Within our computational tool, CFD-ACE, various turbulence models can be used. The more often used, the “k_t-ε_t” model, does not offer very accurate results during transition because it only considers the overall effect of turbulence in the mean flow field. However, when the interest occurs with parameters such as the heat transfer coefficient and the friction factor during laminar-to-turbulent transition, it is suggested to use a Low Reynolds number model. These models permit the integration of momentum and “k_t-ε_t” equations all the way to the wall. The difficulty with them is that the first grid point must be placed in the laminar sublayer (y^+~1) in order to properly connect the laminar sublayer with the log-law (wake) layer. Therefore, this kind of model requires the use of very fine grids near the wall boundaries.

We selected the Low Reynolds number “k_t-ε_t” model from Chien. For more information on this are see (Ref. 29) or (Ref. 30). The “k_t-ε_t” equations have been modified to include the molecular viscosity that dominates in the near wall regions. The general form of the Low Reynolds number models is given by the following equations:

$$\frac{\partial}{\partial t}(\rho k)+\frac{\partial}{\partial x_j}(\rho u_j k)=\frac{\partial}{\partial x_j}((\mu+\frac{\mu_t}{\sigma_k})\frac{\partial k}{\partial x_j})+\rho(P-\varepsilon-D) \quad (23)$$

$$\frac{\partial}{\partial t}(\rho\varepsilon)+\frac{\partial}{\partial x_j}(\rho u_j\varepsilon)=\frac{\partial}{\partial x_j}((\mu+\frac{\mu_t}{\sigma_\varepsilon})\frac{\partial\varepsilon}{\partial x_j})+C_{\varepsilon_1}f_1\frac{\rho P\varepsilon}{k}-C_{\varepsilon_2}f_2\frac{\rho\varepsilon^2}{k}+E \quad (24)$$

$$\mu_t=C_\mu f_\mu\frac{\rho k^2}{\varepsilon} \quad (25)$$

The Chien model parameters appearing in the equations above are:

$$C_\mu = 0.09, C_{\varepsilon_1} = 1.35, C_{\varepsilon_2} = 1.8, \sigma_k = 1.0, \sigma_\varepsilon = 1.3$$
$$f_\mu = 1 - \exp(-0.0115y^+), f_1 = 1.0$$
$$f_2 = 1 - 0.22\exp(-(\frac{Re_t}{6})^2) \qquad (26)$$
$$D = \frac{2vk}{y^2}, E = -2v(\frac{\varepsilon}{y^2})\exp(-0.5y^+)$$

The turbulent kinetic energy was expressed using the turbulent intensity variation, which is provided by the following correlation (Ref. 29):

$$I = 0.16Re^{-1/8} \quad (27)$$

for the core of a fully developed duct flow.

As suggested in (Ref. 29), within internal flow problems, the duct hydraulic diameter is a good choice for a turbulent length scale. Further assumptions/settings included a) zero roughness conditions were set, b) to avoid numerical instabilities, the upwind first order scheme was used for advection, and c) the number of iterations of the solution process was increased in order to achieve the same convergence criteria as in the laminar cases.

2. Transition Region

As the Reynolds numbers increased, it was anticipated for the turbulence parameters to increase. Thus in each simulation, the variation of the y^+ at the wall boundary was examined. In order for y^+ to remain in the order of unity further grid refinement was required. A $y^+ < 1$ was achieved at the lower endwall boundary, but at the pins' surface, y^+ increased with height and with downstream location from the stagnation region as shown in Fig. 15. The larger values of y^+ at increasing height were due to the extrusion power law that was used for the Z dimension during the grid construction. The increase in y^+ along the pins' perimeter can be explained by the acceleration of the flow due to the diffuser's shape region between pins, thus causing a local increase of the turbulence levels. Figure 15 results were obtained at a Reynolds number of 3,500.

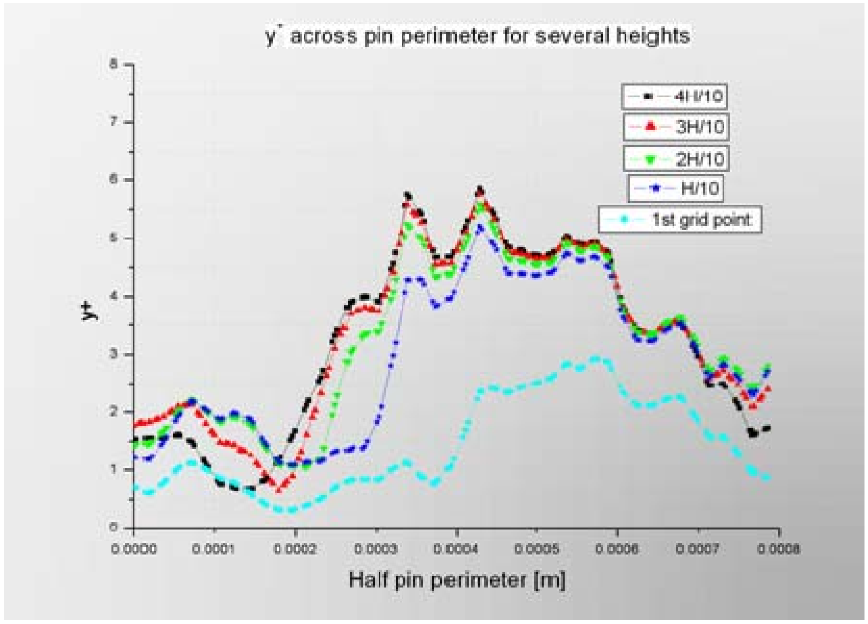

Figure 15. y^+ variation with the half pin perimeter at several heights

Despite further grid refinements and increased number of iterations, it was not possible to reduce the y^+ values. Hence, turbulent models require very fine grids, a lot of computer memory, and even greater amount of computing time. Figure 16 represents a three dimensional carpet plot of y^+ for a z-axis cut of the model for a Reynolds number of 3,500 at z=0.

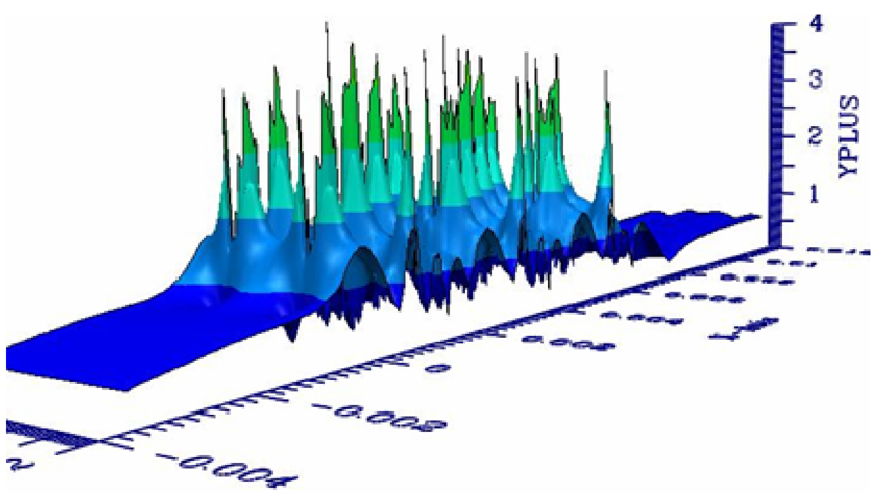

Figure 16. y^+ variation in the lowest cells layer of the model

Also very encouraging from a heat transfer point of view is that the maximum heat fluxes at the pins' surface are met at the 35-40 degrees downstream of the stagnation point. The y^+ in this region is still increasing, because it is the initial region of the flow acceleration. As expected from theory, very similar to the y^+ trends were met for the turbulent kinetic energy.

We try to identify the transition in a plot that compares the effective array heat transfer coefficient with the required specific fluid friction power. This plot fits our purpose well, since it combines both heat transfer and fluid flow characteristics. Figure 17 provides this information for both the laminar and the turbulent models for the Reynolds numbers between 1,000 and 8,200.

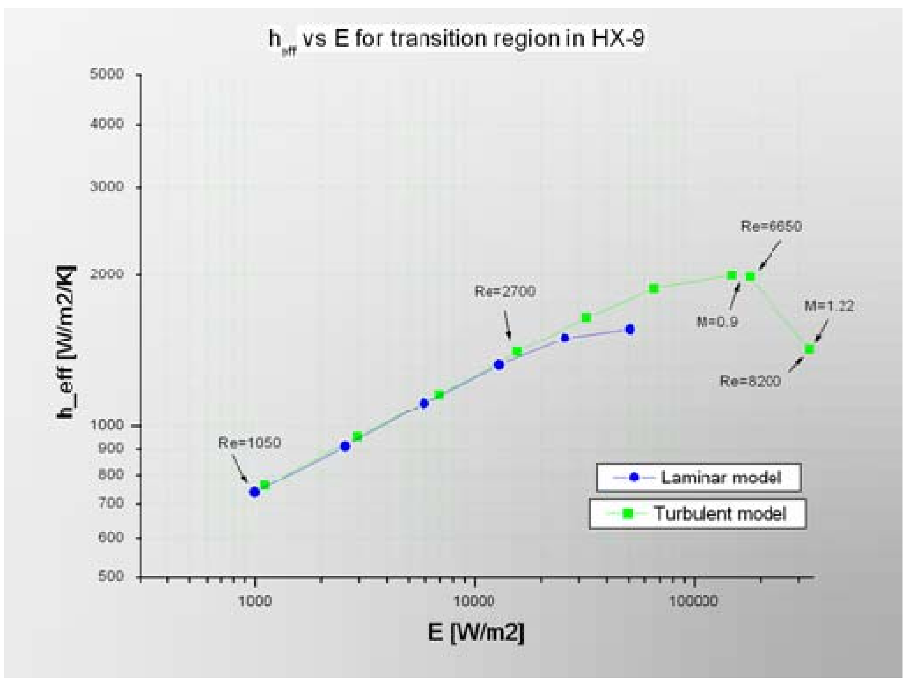

Figure 17. Comparison of laminar and turbulent models for HX-9

Both models overlap until Re > 2,000. After that point the laminar model under-predicts h_{eff}. In the configuration of Hamilton (Ref. 7), the fall of the laminar model occurred at Re > 1,000. Therefore, first estimates indicate that transition occurs in different regions for different configurations and depends on the area density of every array. For heat exchangers with smaller area magnification factors the transition region is shifted toward higher Reynolds numbers. At even higher Reynolds numbers shock waves are formed. This will be examined more extensively in the following chapter.

The Nusselt number follows similar trends as the heat transfer coefficients, therefore Nusselt numbers decay near and after the shock regions. The shock wave problem was somewhat expected due to the micro-scale character of the exchangers. When comparing micro- with macro-scale heat exchangers at similar Re numbers, the micro-scale heat exchangers have to operate at higher velocities, which give rise to the shock problems. But since CFD–ACE is not a robust compressible solver, it is not very reliable for analyzing problems at these high velocities. Consequently, we use the results of the turbulent model until a Re < 6,200, where the maximum Mach number was approximately 0.83.

Another aspect that has to be examined is the variation of the effective viscosity. We found that the effective viscosity reached and exceeded values five times greater than the laminar viscosity in the core of the flow (upper symmetry plane boundary condition) in a regime of the Reynolds numbers around 2,000. Figure 18 presents a carpet plot with the effective viscosity values for a z-axis cut of the array just below the upper symmetry boundary of the heat exchanger for the Reynolds number around 2,000.

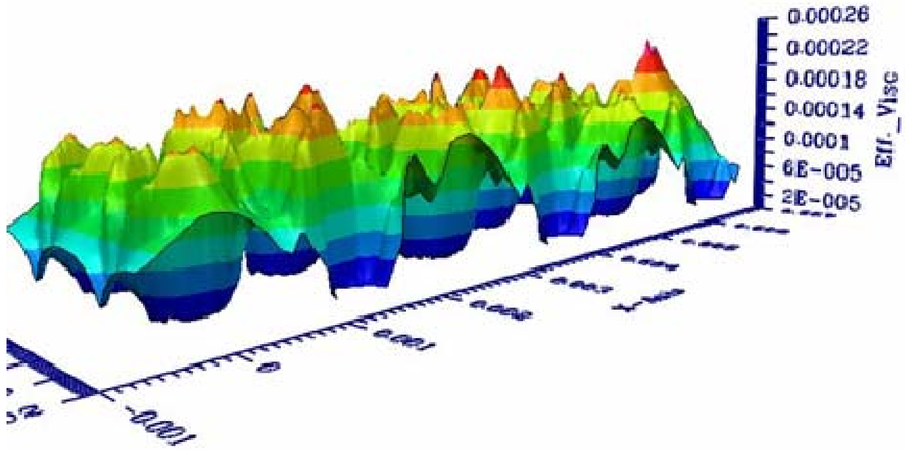

Figure 18. Variation of effective viscosity in the HX-9 for Re=2000

It is generally suggested that when this criterion has been reached, the modeling must switch into the turbulent regime.

D. EXPERIMENTAL CORROBORATION

1. Validation with Historical Data

As discussed above, the current CFD results were compared to existing experimental data. Such experiments used the same configuration (X/D=S/D=2.5, H/D=1) from, Chyu (Ref. 10) and Metzger et al. (Ref. 6). Chyu et al (Ref. 12) conducted an experimental work based on a well known mass transfer technique, the naphthalene sublimation experiments, and through the use of the mass transfer analogy, obtained heat transfer results. The difference between Chyu and the current study are the following definitions: Chyu's Reynolds number was defined as follows:

$$Re = \frac{\rho V_{max} D}{\mu} \quad (28)$$

where V_{max} is the average flow velocity in the minimum flow area (between a pins row) and D is the actual pin diameter.

Chyu defined the Nusselt number as follows:

$$\mathrm{Nu} = \frac{hD}{k} \quad (29)$$

where, again, D is the pin diameter and h is the heat transfer coefficient that comes from:

$$h = q''(T_{wall} - T_{bulk}) \quad (30)$$

where q'' is the heat flux and T_{bulk} is the bulk temperature in the channel based on the mass transfer analogy. Because it was impossible to equate their T_{bulk} using the information provided in their paper, and because the bulk outlet temperature used in the current study (the net outlet temperature of the coolant fluid,) was not consistent with theirs, it is better to compare their Nu number results with a slightly modified version of our Nu number (where the pin diameter is used instead of the hydraulic diameter.) The results can be compared by examining Table 7 and Figure 19.

Table 7. Data comparison of present study with Chyu et al (1999).

Re_{Dh}	Nu_{Dh}	Present study Re equivalent	Present study Nu equivalent	Nu from Chyu et al correlation
1033	19.7	969	14.3	17.6
1498	24.7	1406	17.9	21.9
2067	30.0	1939	21.8	26.4
2790	36.4	2617	26.4	31.5
3617	42.7	3393	30.9	36.6
4650	48.7	4362	35.3	42.4
6200	51.8	5816	37.5	50.1
6613	51.3	6204	37.2	52.0
8267	36.9	7754	26.7	59.3

The correlation that Chyu provides is $\mathrm{Nu} = 0.32\mathrm{Re}^{0.583}$ for Re>6000. The above extracted data is from an extension of their correlation toward lower Re numbers because our micro heat exchanger could not reach their higher Reynolds due to the shock wave issues.

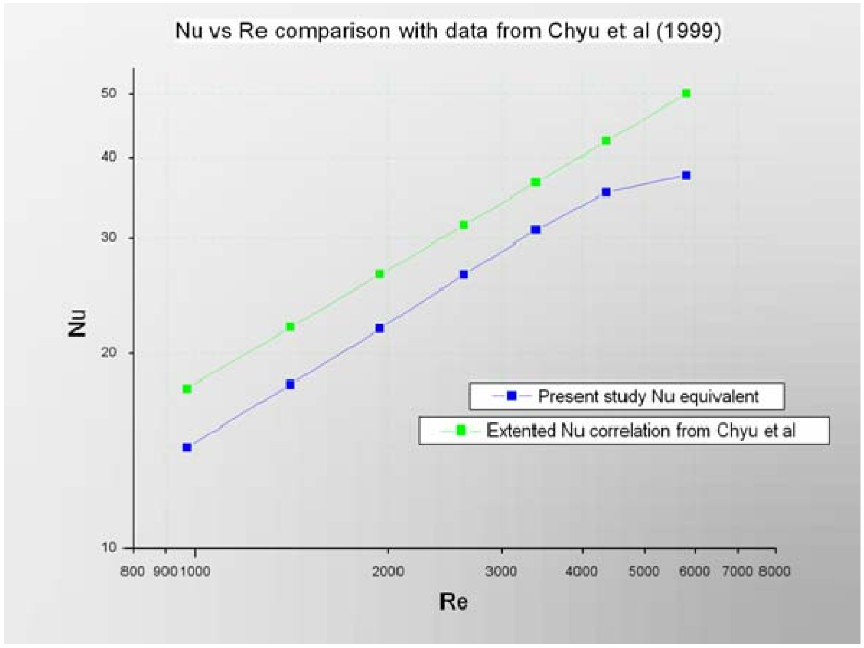

Figure 19. Nu vs. Re comparison with historical data for HX-9

If we consider that Chyu tested an array with 7 rows of pins and the current CFD model for HX-9 had only 6, the difference in the definitions of the Nu number and other parameters (such as the viscous dissipation not being included in this study,) the agreement and the scale of the findings is sufficiently satisfactory. Moreover, the parallel trend that the two curves of the compared data are following is a very positive result.

By comparing our findings with Metzger et al. we again achieved a very similar trend, with smaller differences of about 15%. Metzger used the same definition as Chyu et al. for the Re and Nu numbers, while his heat transfer coefficient was derived from the equation

$$h = \frac{q/A_{wetted}}{(t_{wall} - t_{ref})} \quad (31)$$

where for the t_{ref} definition and computation the reader is referred to (Ref. 6). The fact that the computational model's trend-line develops in the region between the two predictions of the two empirical researchers, is very positive for the performance fidelity of the model.

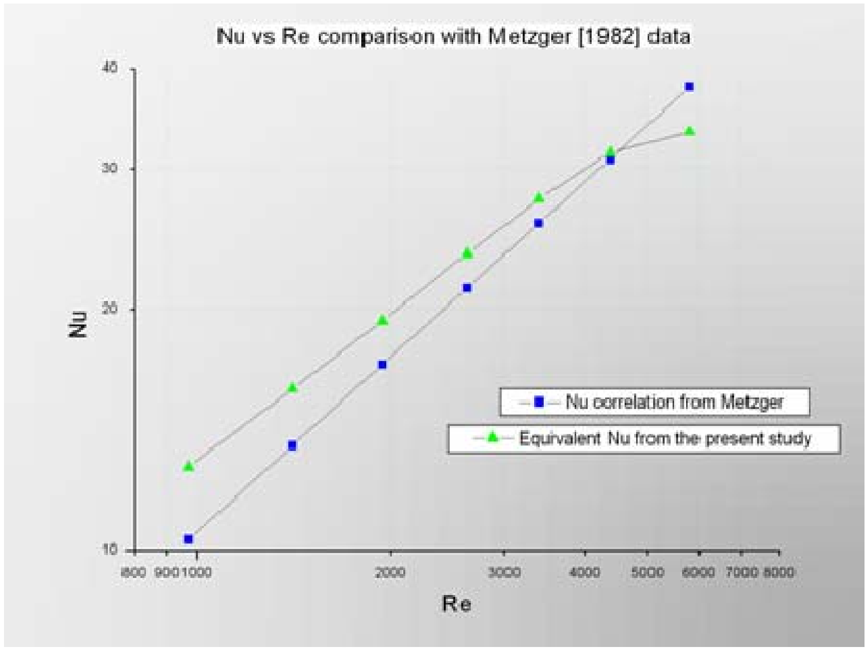

Figure 20. Comparison of Nu as a function of Re with Metzger's results

Also Metzger in his study, found that the average Nusselt number decrease after the sixth row is negligible for this configuration and it can be taken as if it has reached a steady value of an infinite length array.

In an earlier study Chyu (Ref 28), also researched the pressure losses and the friction factor for the same specific configuration. He defined the friction factor as follows:

$$f = \frac{2\Delta P}{\rho V_{max}^{2} N} \quad (32)$$

where ΔP is the pressure difference between the inlet and exit sections of the array, N is the number of pin rows and the V_{max} is defined as above. His findings are presented in figure 20.

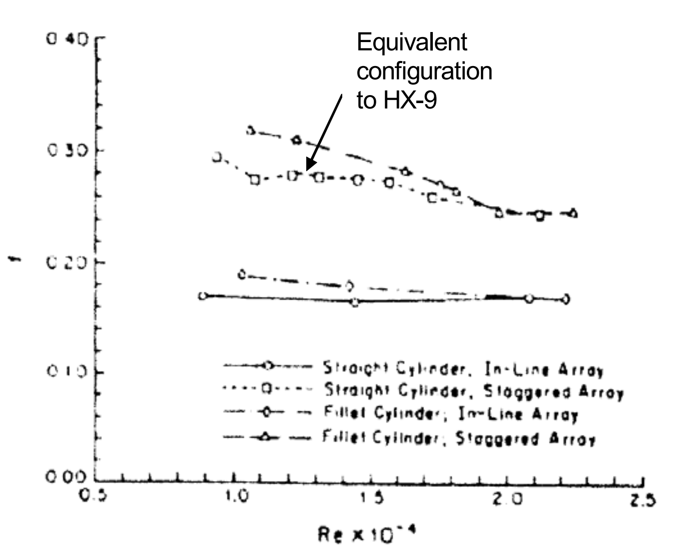

Figure 21. Friction factor vs Re from Chyu [1989] for X/D=S/D=2.5, H/D=1

The present study produced equivalent parameters depicted in figure 21 - agreement is excellent! Chyu's experimental array consisted of 7 rows of pins and appears that this difference did not have the influence that the Nu number results showed.

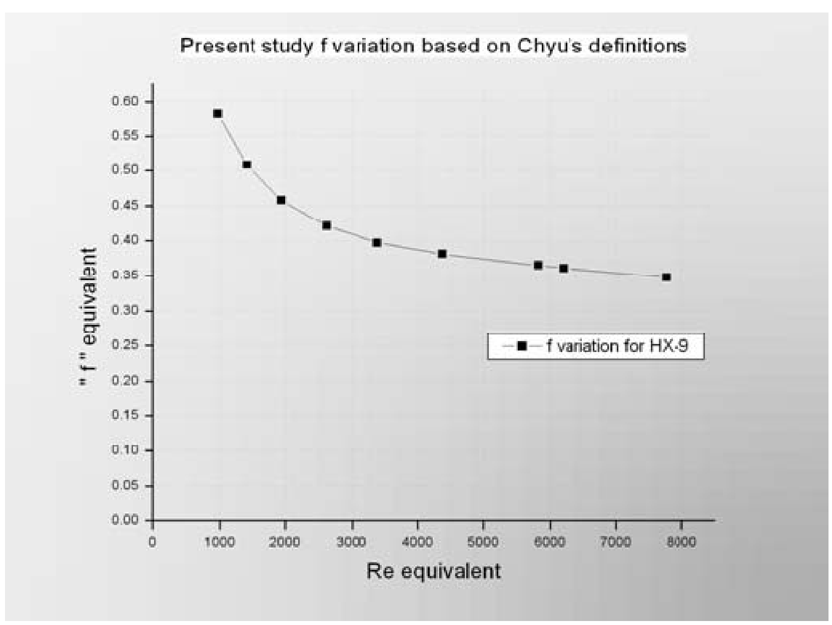

Figure 22. Friction factor variation of the turbulent model for HX-9

Marques et al. (Ref. 16) tested the same configuration as Chyu et al., but in the micro-scale. Marques' pin diameter was 500μm, the same as to the current study. Accordingly, the HX-9 design is identical with the design of Marques, but with one row less. Also because Marques et al. heated only the one endwall, we could not compare the present study's heat transfer findings with theirs. However a comparison of the friction factor could be very useful. After they corrected the parameters, they validated their results against Chyu's study, as shown in figure 23.

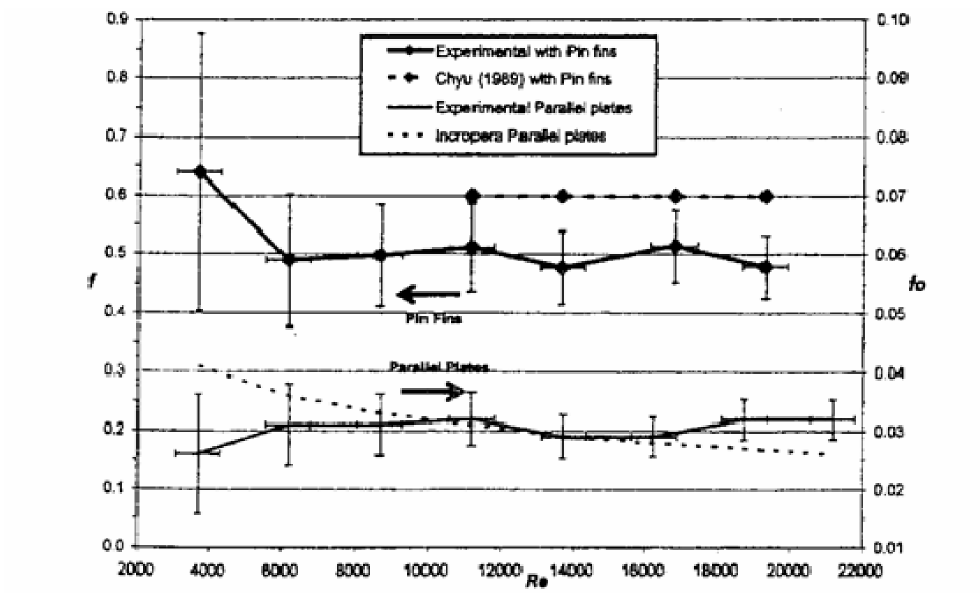

Figure 23. Friction factor as a function of Re number from Marques [2004]

Consequently, there is a very similar trend for the values of the friction factor predicted above which seems to tend towards a constant value at Re > 6,000. This corresponds to a value of Re > 5,000 in the current study.

2. Validation with NPS Experimental Research

Roussakies (Ref. 17) and Bosserman (Ref. 18) conducted experimental research using identical configurations to the current study. Roussakies worked with configurations exactly similar to HX-1, 2, 10 while the Bosserman tested all of the current configurations except for HX-7,8 and 9 due to problems with blockage effects of the arrays' passage ways. Therefore, only HX-1 and 10 were validated against their results.

Bosserman's results of the friction factor for some of the HXs like 3, 4 and 6, in which he found numbers of $15 < f < 100$ for Re=100, indicate trends that can only be explained by the heat exchangers being clogged (not properly released.)

Figure 24 plots the Nu for the first heat exchanger for a range of Re.

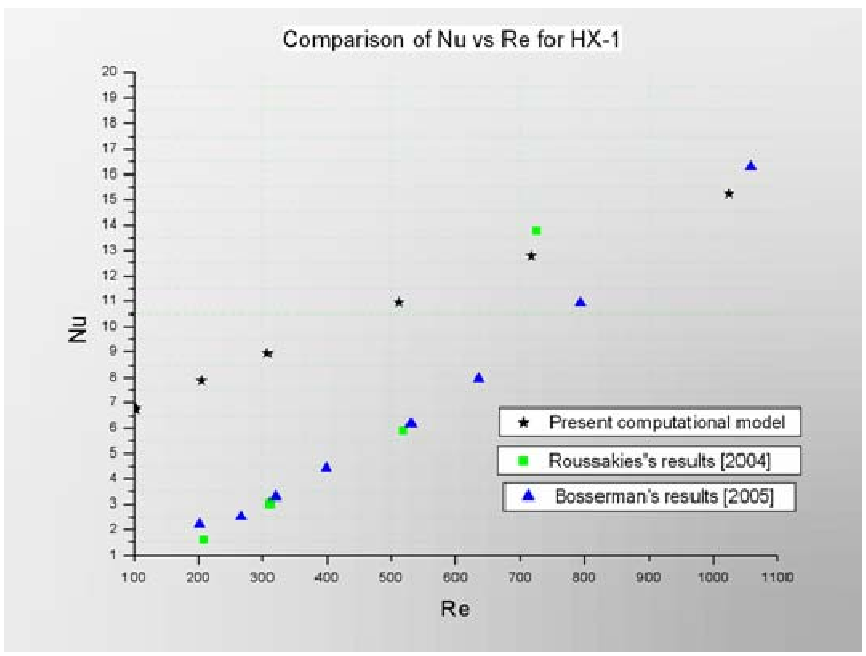

Figure 24. Comparison of Nu vs. Re for HX-1 with experimental work

From the plotted data, we have good agreement for Re > 600, where the points are shown converging in a similar trend. We noticed a similar deviation with the Nu results for the average array heat transfer coefficient when it was plotted as a function of specific fluid friction power. This was expected, since both parameters are in great dependence.

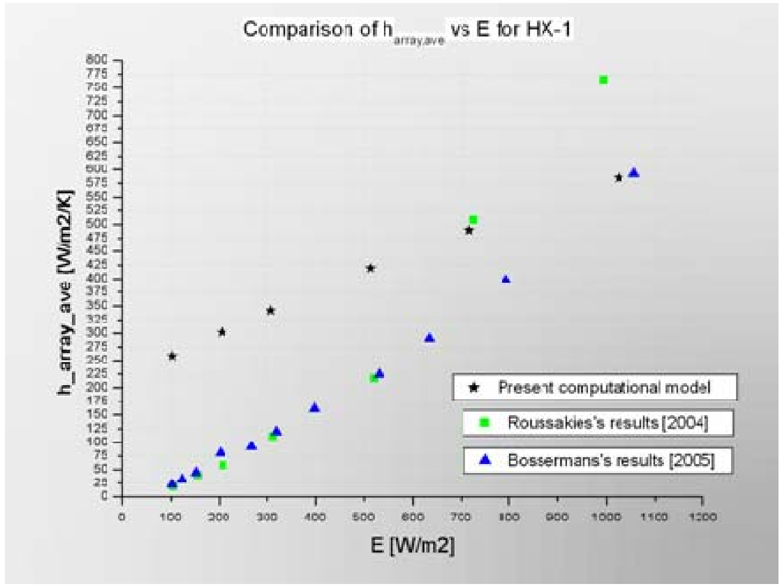

Figure 25. Comparison of $h_{array,ave}$ vs E for HX-1 with experimental work

Regarding the friction factor, our findings were again corroborated. Our results were found to be between the trends of the experimental results. Even more positive is the fact that the data showed similar decay as the Re increased – shown in figure 26.

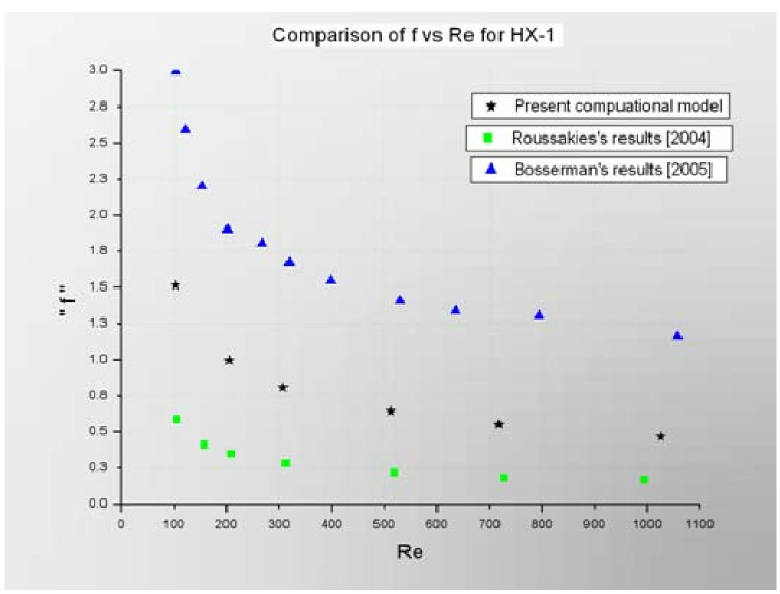

Figure 26. Comparison of f vs Re for HX-1 with experimental work

The comparison of HX-10 with experimental data led to stronger corroboration, especially with Roussakies's findings. His Nu variation with Re is closer to the computational model results than Bosserman's.

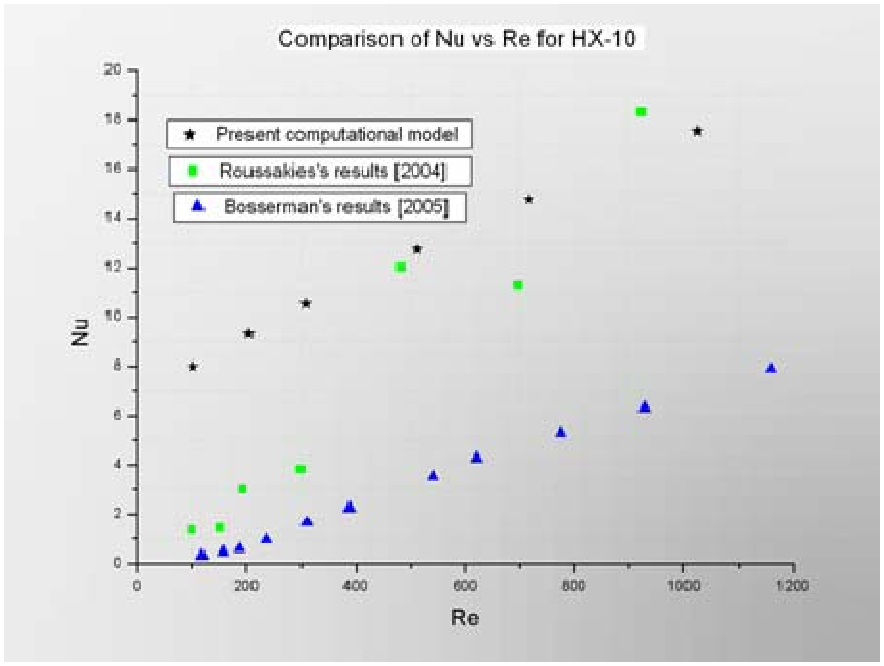

Figure 27. Comparison of Nu vs Re for HX-10 with empirical data

Roussakies predicted values for Re > 400 close to the numerical model's trend-line. In his data, the same behavior is seen in the average heat transfer coefficient values. This happens according to figure 28, for low friction power values, as compared to Bosserman's results, which also predict a well established agreement for the friction factor. The trends between Roussakies and our model in figure 29 are extremely similar and the values are very close. The predicted friction factor values are almost identical for a region of Re > 400.

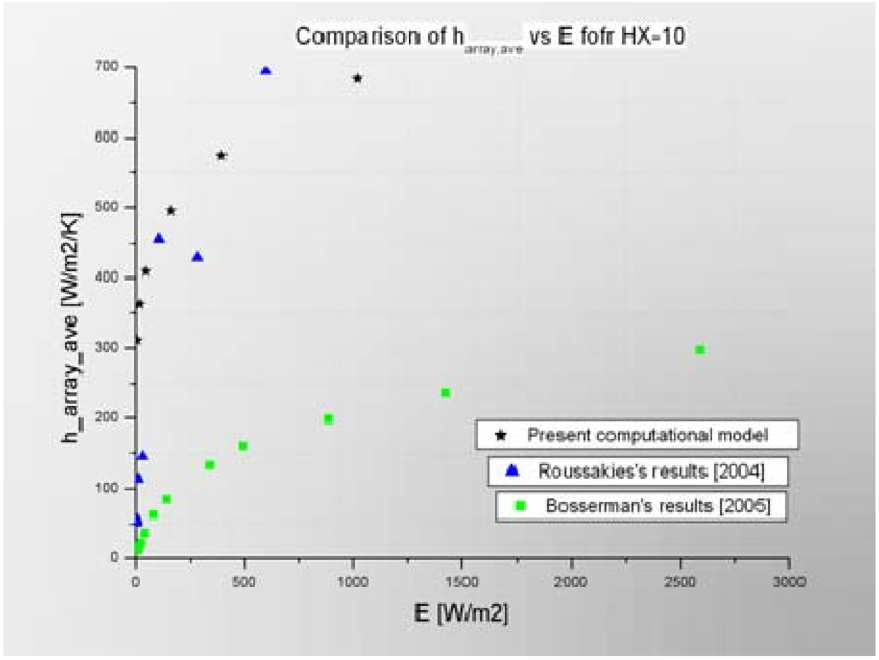

Figure 28. Comparison of $h_{array,ave}$ vs E for HX-10 with empirical data

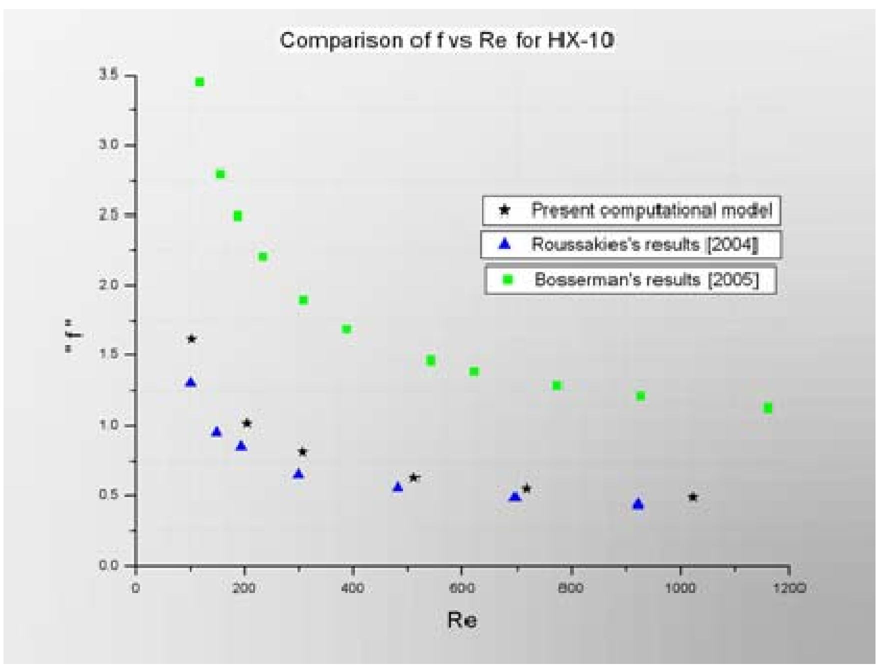

Figure 29. Comparison of f vs Re for HX-10 with empirical data

Consequently, the computational models of the heat exchangers that have been developed and are discussed in this chapter, produced results very similar to earlier experimental data in the macro-scale, where a suitable correction was applied, and extremely similar where the accurate equivalency from their definitions was known and has been implemented. As to the comparison with the micro-scale results, we are sufficiently satisfied with the existent corroboration.

Therefore, based on the validation by both the micro and the macro scale data, the results of the macro-scale experiments can be directly applied to micro-scale heat exchangers.

THIS PAGE INTENTIONALLY LEFT BLANK

IV. RESULTS-DISCUSSION

Here we discuss selected performance characteristics of the heat exchangers that were analyzed (shown in Table 3) which for convenience are divided into two sets according to their pin diameter. The characteristics are chosen to highlight various features of the behavior of the heat exchangers.

A. HEAT TRANSFER FLUX, RATE, AND COEFFICIENT

The heat transfer coefficient is one of the most critical and interesting of the examined parameters. Since it was not possible to directly examine the behavior of the local heat transfer coefficient in CFD – VIEW, we inspected heat fluxes and heat transfer rates instead.

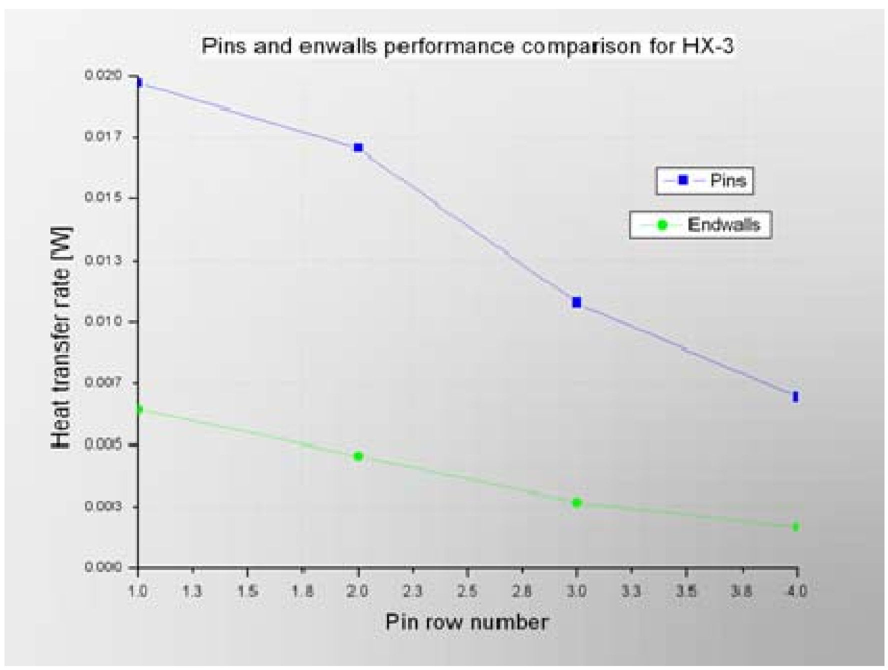

Figure 30. Pins and endwall heat transfer comparison for HX-3

HX-3 was found to be one of the best performers, since it had a very packed configuration but a bigger pin diameter. The contribution of the endwall and the pins to the heat transfer, along the total length of the array is compared in figure 30 for Re=500. It can be seen that for the first row of pins the heat transfer rate achieved values more than 250 percent greater than the endwall, which was reduced greatly for the following rows without any great alteration in the percentage difference contribution. To confirm that result, we should inspect the heat flux distribution at those wall boundaries. The endwall showed very high fluxes for the very initial part of the Hx, but reduced very quickly and with a very high gradient along the stream-wise distance as is presented at the figure 31.

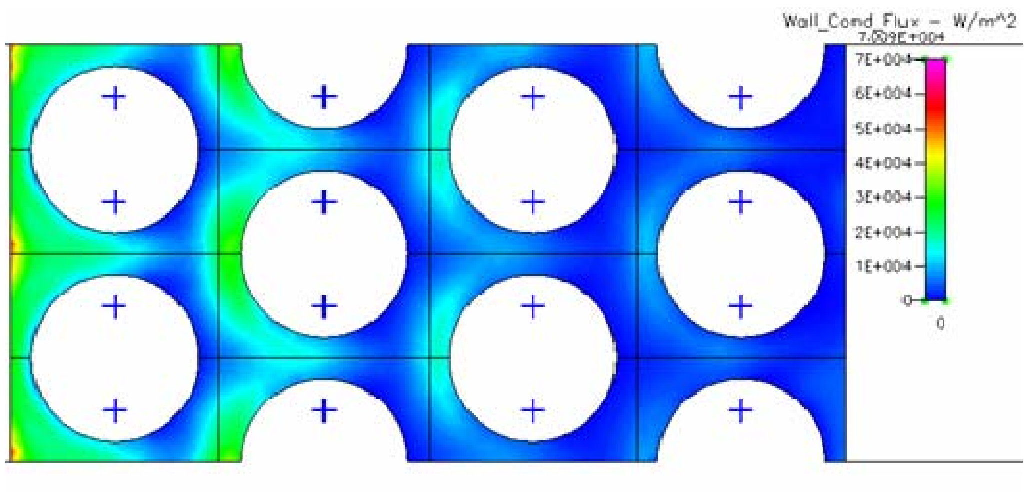

Figure 31. Endwall's heat flux distribution in HX-3

After the first row the values of the actual wall flux were falling to a level of 10,000 W/m^2. On the other hand when we examined the heat flux according to pin chord-length in the first row for several heights, we noticed that it reached near maximum values from almost a quarter of the half height which was modeled. This means that the pin keeps the highest achieved heat flux values for more than 75 percent of its length. Furthermore, the maximum values for the heat flux reached are around 35-40 degrees downstream from the flow direction angle and are maintained until 100 to 105 degrees, from which point they start to reduce dramatically due to generation of vortex shedding and recirculation effects. Figure 32 is a plot of this behavior with angle from the forward flow direction to 360 degrees around a pin.

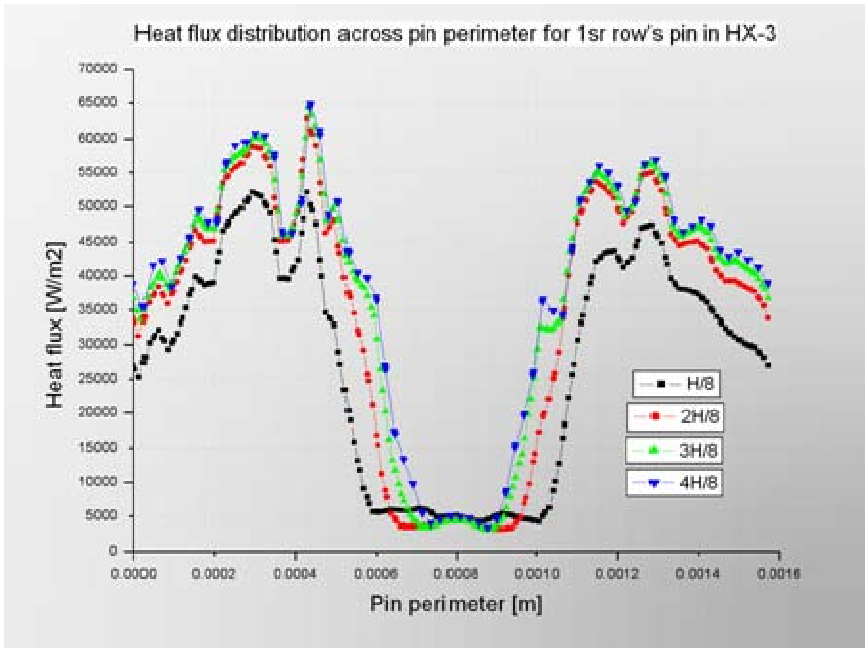

Figure 32. First row's pin heat flux distribution for several heights in HX-3

It is worth noting the scale of the heat fluxes presented and the great potential of the micro heat exchangers to dissipate large heat fluxes. The values of heat flux that the pins reach are extremely high and were highest for the second row as illustrated in figure 33.

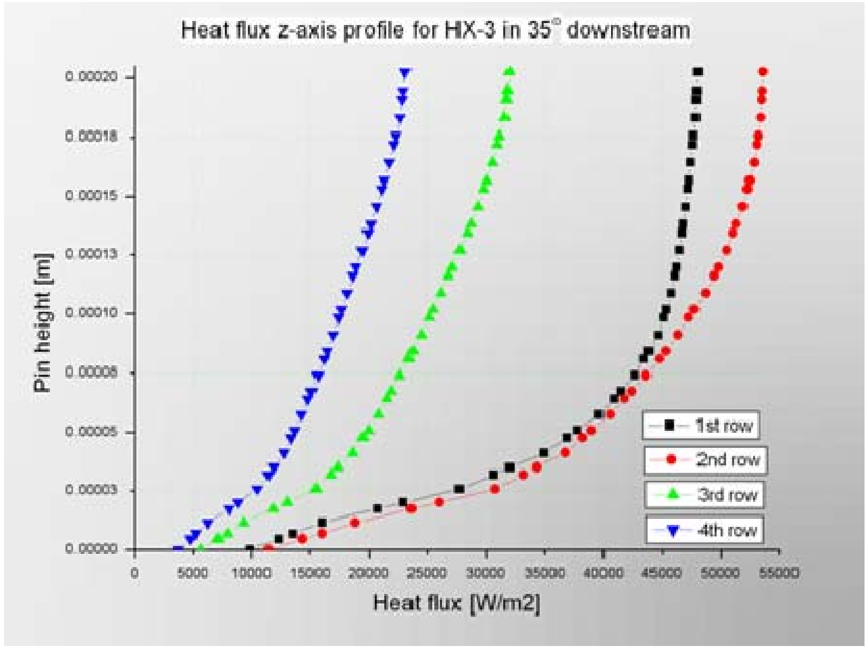

Figure 33. Heat flux z-axis profile for 35^o downstream the pin surface

After the second row, the values of the heat flux were reduced, but not with rates as high as those for the endwall. The second row was the one that clearly achieved the greater values and this is probably happen due to the acceleration of the flow after passing the first row, due to the nozzle effect which drives it more toward the next row's pin center. In figure 34, which presents the contour distribution of the heat flux in a first and a second row pins, the red region of higher flux values has shifted toward the stagnation point for the second row pin compared to the one of the first row. However, the first row finally produced bigger heat transfer, when we look back at the comparison plot for the pins and endwall. This could be explained by the reason that the first row pin achieved greater area average heat flux values.

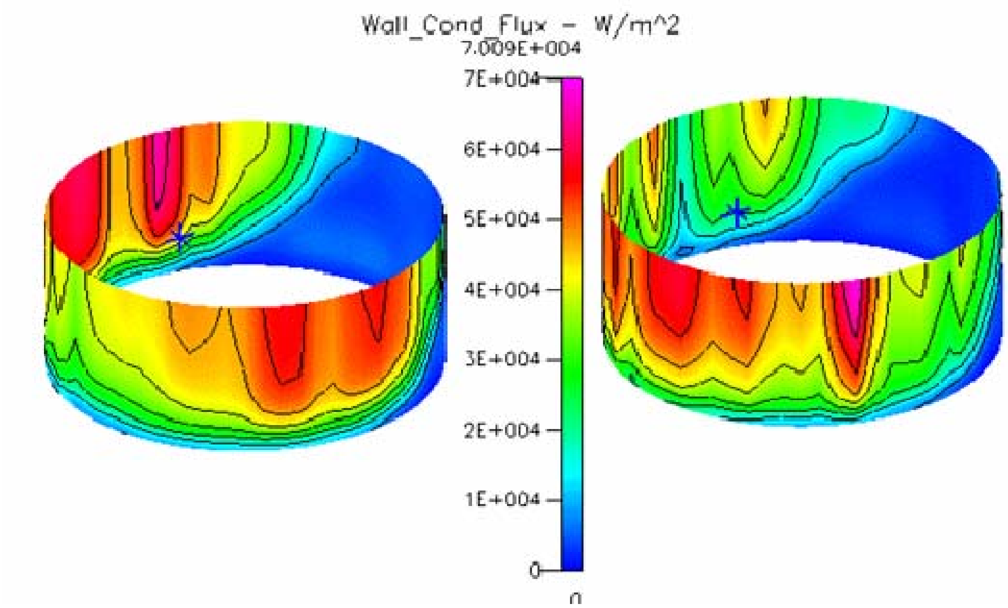

Figure 34. Heat flux contour plot of 1st and 2nd row pins in HX-3

By averaging the heat flux values at these two pin surfaces using the calculator tool of CFD – VIEW we confirmed that result, but as we checked and for other arrays, we found that it did not happen in all the configurations. Also, because the great difference in the heat transfer participation, that pins and endwall resulted it was important to inspect how other configurations behaved. In a comparison for a Reynolds number equal to 500 for HX-1, we got opposite results to those in HX-3. In HX-1, the endwall provided more heat transfer, but not with as much difference as the pins did in HX-3.

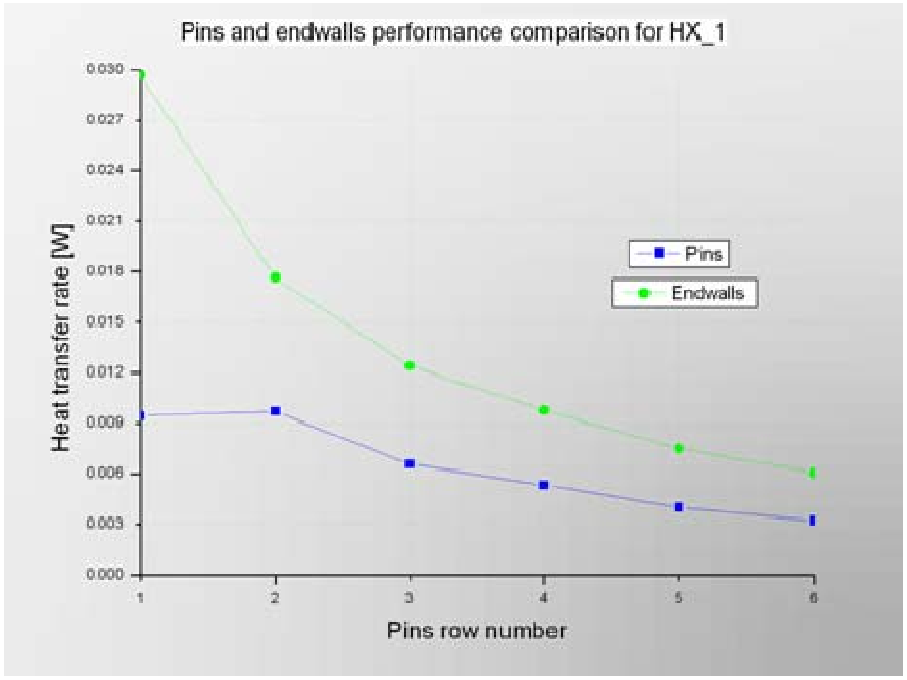

Figure 35. Pins and endwall heat transfer comparison for HX-1

The greater differentiation is found in the contribution of the first row, and as we checked the following rows, we noticed that this difference dies quickly, mostly due to the more general wall behavior. The pins continue to contribute a high enough amount, as compared to their initial amount of heat transfer. At this point, we should mention that HX-1 did not return the greater heat transfer coefficient, as compared to the other arrays. To get a total picture of this matter, we examined HX-2 which has the increased span-wise ratio S/D. The participation in this array was comparable for both - the endwall produced greater heat transfer in the first row only while the pins prevailed in the following rows with their more constant performance.

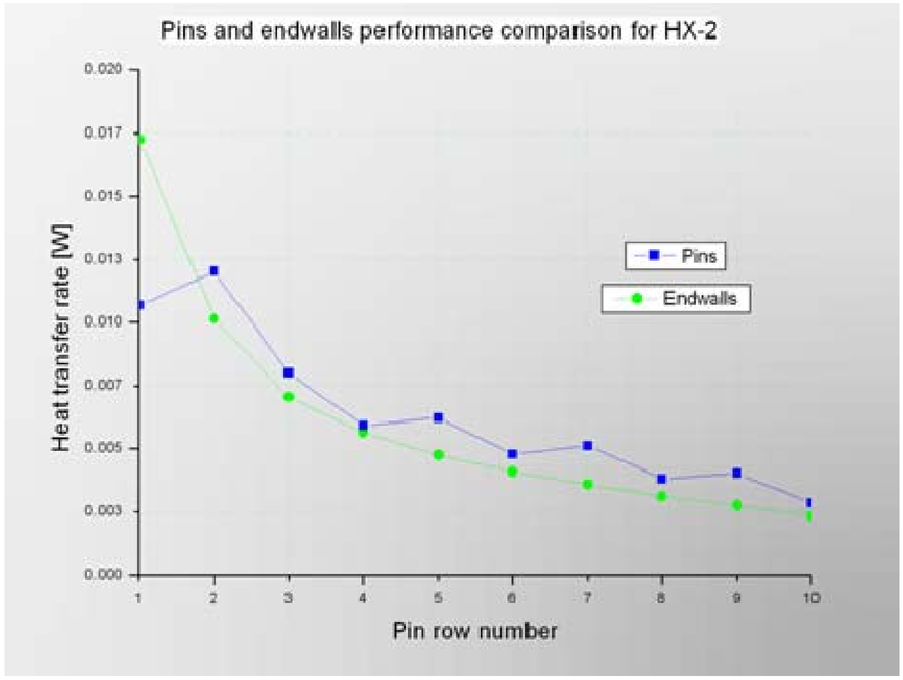

Figure 36. Pins and endwall performance comparison in HX-2

The pins produced a 20 – 30 percent greater heat transfer from row 2 to row 10. Consequently, the pins and endwall contribution is not constant; in fact, it is strongly dependent upon the configuration. More specifically if we examine the area magnification factor of the inspected arrays, we can state with great assurance that the pins' participation depends on the area density of every array. Thus, in HX-3, with the higher area density, the pins contribute the greatest in a comparison of the three arrays.

Furthermore, in both HX-1 and HX-2, the second row of pins produced the greater heat transfer rate in contrast to HX-3. Accordingly, which row produces the maximum average flux and subsequently which row dissipates more heat is something varied, and depends upon the configuration too. However, the heat flux in all of them reached its maximum local values in the second row. The result that the second row achieved the higher local heat fluxes is supported by figure 37 which is a plot of the flux distribution at the upper symmetry plane along the pin chord-length for all rows of HX-1.

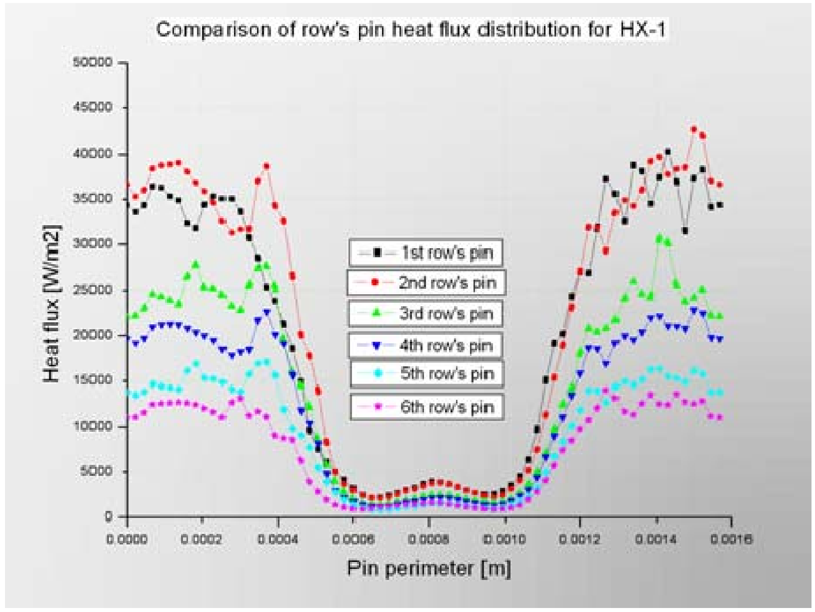

Figure 37. Heat flux distribution for the pins of HX-1 at the core of the flow

However, in order to make a more fair judgment of the pins and endwall contribution, we use a chart that illustrates the attained average heat fluxes of every row, which are independent of the flow wetted area factor, as in figure 38.

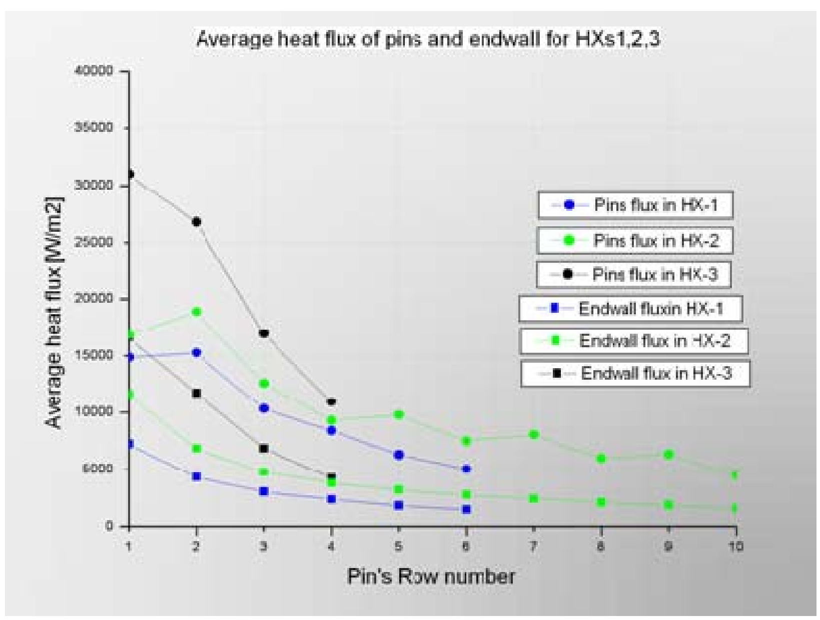

Figure 38. Heat flux comparison of pins and endwall in HXs1, 2, 3

Here we can observe that the difference in the first three configurations varies from 50 to 250 percent, based on the endwall values. Moreover, it shows more clearly that the performance of the pins is more generally dependent on the heat exchanger's wetted area magnification factor. In addition, it is clear that the second row does not always accomplish the highest flux as happens in HX-3.

For the average heat transfer coefficient for the two sets of arrays, figures 39 and 40 present their variation with Reynolds number. It is clear that HX-3 and 7 achieve the greatest values in the higher Re number regime for the two sets.

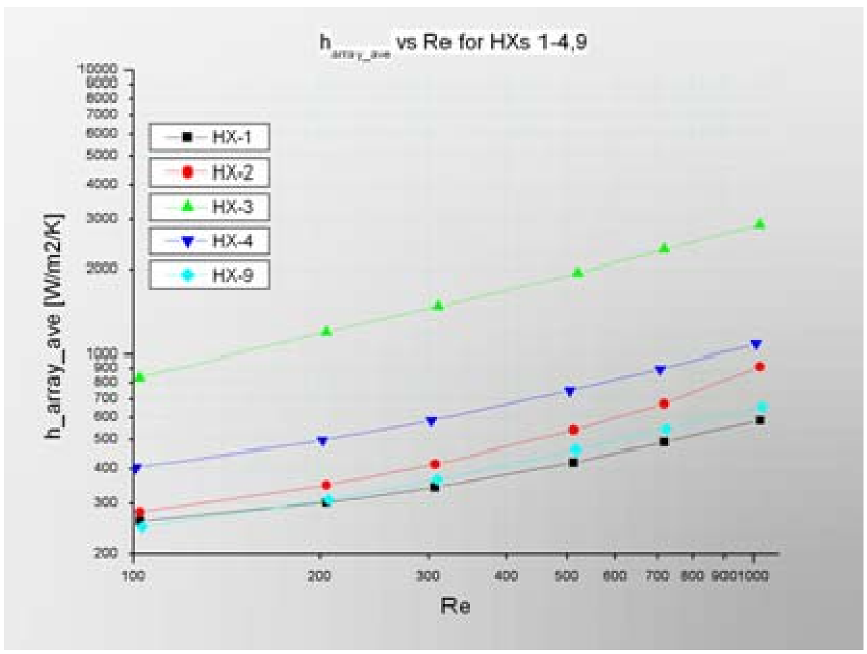

Figure 39. Average heat transfer coefficient vs Re for HXs 1-4,9

From a more total view, exchangers 6, 7, and 8 reached the higher coefficients, which might have been expected since they have the greatest area density. When we inspected the first set, HX-4 (X/D=3, S/D=1.25) was found to have greater performance, compared to HX-2 (X/D=1.25, S/D=3), suggesting that the stream-wise spacing variation proved to have a greater effect compared to span-wise distance. This result is consistent with the theory, since in HX-4, the flow is forced to follow a more circuitous path around the pins and, as a result, to increase the interaction with them. In HX-2 with its wider passages, the gain in the heat transfer is not so significant, since the flow has greater direct through-flow regions at the side of the pins. Also worth noting are the values for HX-3 which are far higher in the figure than all the others. The combined reduction in both spacings, stream-wise and span-wise, was the main thing that forced the third configuration to perform so much better than the others and to attain a similar performance as HX-6 and 8 with the small pin diameter.

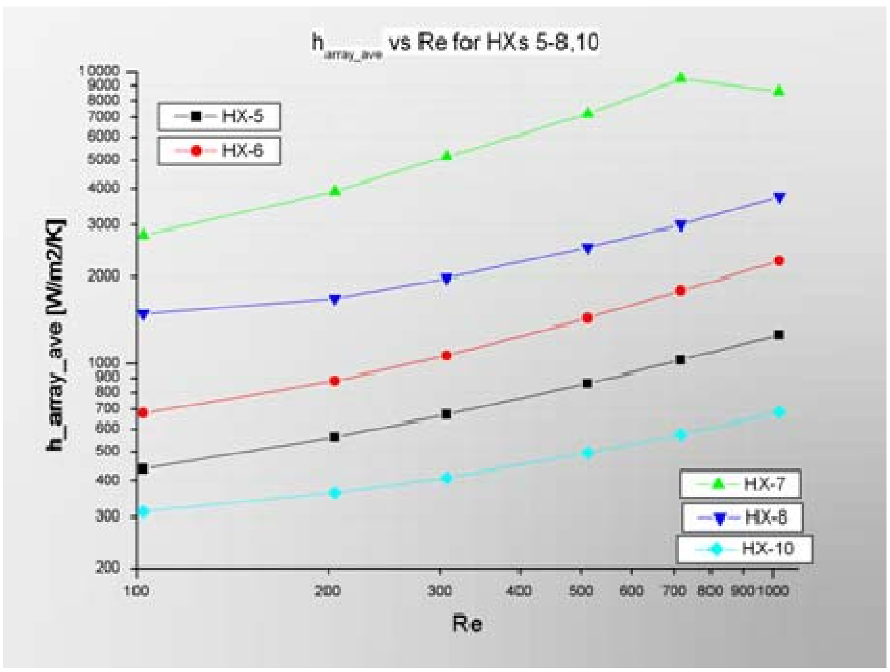

Figure 40. Average heat transfer coefficient vs Re for HXs 5-8,10

In the second set of Hx, the pin diameter was around three times less, which resulted in an increased H/D ratio. This was due to the constant height channel that we kept for all the configurations. In comparing the two plots of the two sets, it is easily noticeable that the main trends of the performance that have been commented on previously are qualitatively the same for the second set, but with a great change in between the configurations' quantitative relation. This is very significant, since it proves that the alteration of one of the three ratios, the pin height to diameter ratio, had a significant effect on the resultant performance. Thus the optimization of the micro heat exchangers is not so simple since it involves a complicated interaction of the different length ratios in the Hx.

It is also important to note that the increase in the H/D ratio had an amplification effect on all of them, but with a different factor for every one of the exchangers as seen from the above discussion.

A chart plotting the heat transfer coefficient versus specific fluid friction power, based on wetted area would be very useful in order to evaluate the performance.

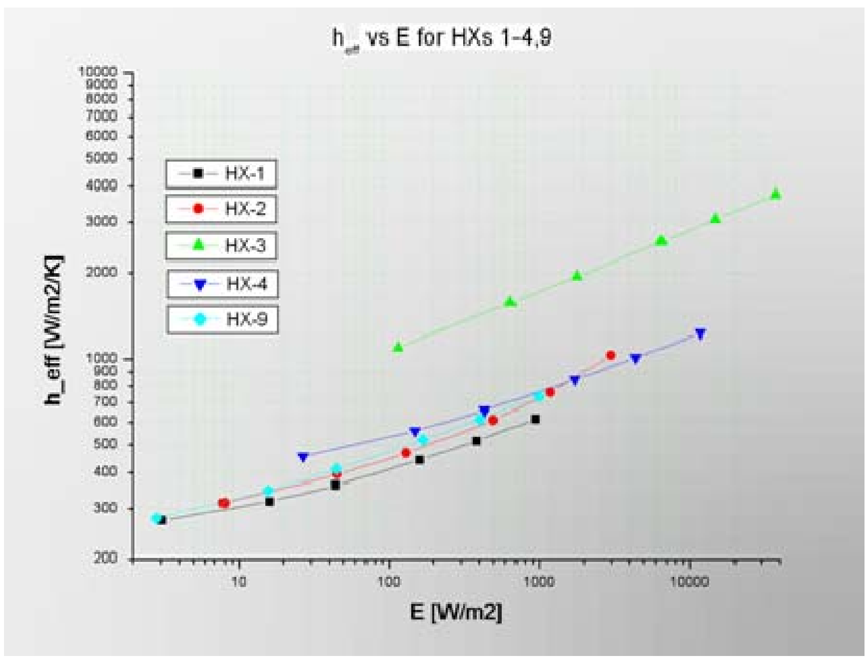

Figure 41. Performance comparison for HXs 1-4,9

The optimum Hx would be one that maximizes the heat transfer rate while minimizing the frictional losses in the flow. For the first set of arrays figure 41 provides that information. Instead of comparing the average heat transfer coefficient, we selected the effective one, because it better represents the actual heat transfer gain from every configuration, since it was derived by taking into account the magnification due to the array area density. The plotted points on each line are for increasing Reynolds number values of 100, 200, 300, 500, 700, and 1,000 in the direction of increasing E.

Between HXs 1, 2 and 9 there is no great difference, except that the second one which, for the same Re values, reaches slightly higher values of heat transfer coefficient, with the analogous required energy, than the others would demand operating at a similar point. However, HX-3 and HX-4 have a great difference between them, with the fourth starting from a value for the h_{eff} of 450 $W/m^2/K$ and reaching a maximum of 1,000 and the third starting from that point and reaching the amount of 4,000 $W/m^2/K$ for the same Reynolds number. If we consider that, for the heat transfer coefficient near 1,000, one demands 100 times more power to drive the flow, we can see that there is a great difference between their performance.

HXs 2 and 4 are closer with the fourth one performing better until a value of Re equal to 500, whereas after this point, HX-2 produces slightly (maximum 30 percent) smaller values of heat transfer coefficient while demanding around three to four times less energy to operate.

In the second set of inspected configurations, all the plotted performances have moved toward the right upper region of the chart except for HX-10. Furthermore, it is interesting that their differentiations are scaled similarly in both figure's directions for all of them except HX-7. The most impressive characteristic of this comparison is the heat transfer coefficient values that HX-7 reached considering its higher area density. But the tremendous amount of fluid friction power needs to be compared to all the other arrays. The deterioration in its performance was clearly noticeable when it approached the shock wave operation region, as the heat transfer reduced while the required specific power grew from 200,000 to almost 500,000 W/m^2.

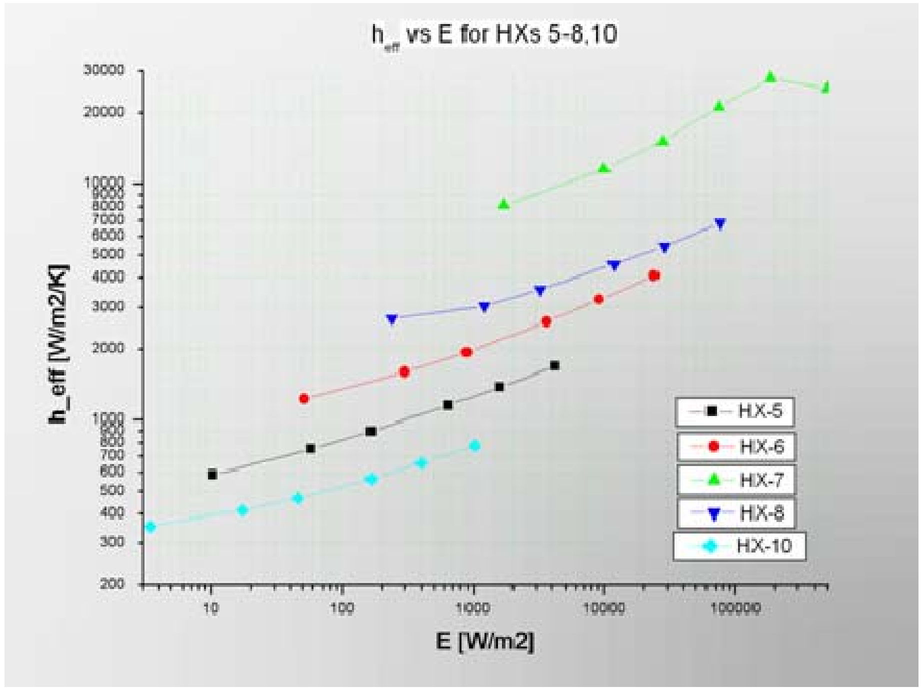

Figure 42. Performance comparison for HXs 5-8,10

To increase the heat transfer performance, it is much more cost effective to move upward in the diagram to a more packed configuration, instead of changing the flow attributes and increasing the Reynolds number.

Also, if we consider HX-1 and 10, which have almost identical performances but differ a lot in their geometrical characteristics, the gain from increasing the H/D ratio in the tenth has been diminished by the increase of the other two spacings, X/D and S/D, as compared to the first array. This is an indication that the height to diameter relation has a stronger influence compared to the other two ratios, and thus needs more attention in the optimization process.

Another way to inspect the heat transfer performance of the tested configurations is to compare them against the performance of the similar dimensions empty duct. Thus in this case, it can be examined the difference that the presence of the pin made, not only by contributing with their surface but enforcing the flow to follow the more tortuous paths around them and increase the heat dissipation of the wall boundaries.

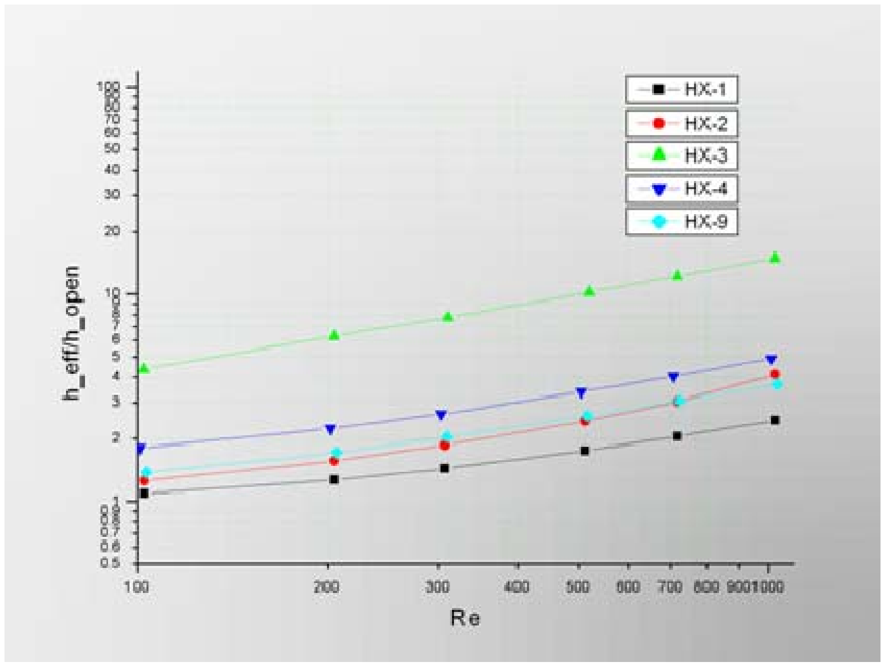

Figure 43. Variation of arrays' effective heat transfer coefficient over the empty duct for HXs 1-4,9

Figures 43 and 44 provide the ratio of the effective array heat transfer coefficient over the corresponding of the empty duct for various Reynolds numbers. The empty duct heat transfer coefficient came up after taking in account the constant Nusselt number of the infinite width square duct, which is equal to 7.54 for the thermally developed flow, as it is reported by Kays and Crawford.

The configurations like HX-3, 6, 8 achieved from five to almost thirty times greater heat transfer coefficients when consider their corresponding empty duct, but the HX-7 returned values of the order of thirty to more or less one hundred. This, as we will examine the friction factor in a following section, was not without an admirable energy requirement that almost forbids any thoughts of applicability that can this configuration would provide.

Furthermore, the fact that for the arrays the heat transfer coefficient increases significantly by increasing the flow characteristics (Reynolds number), which does not occur so intensively for the case of the empty duct, is also important.

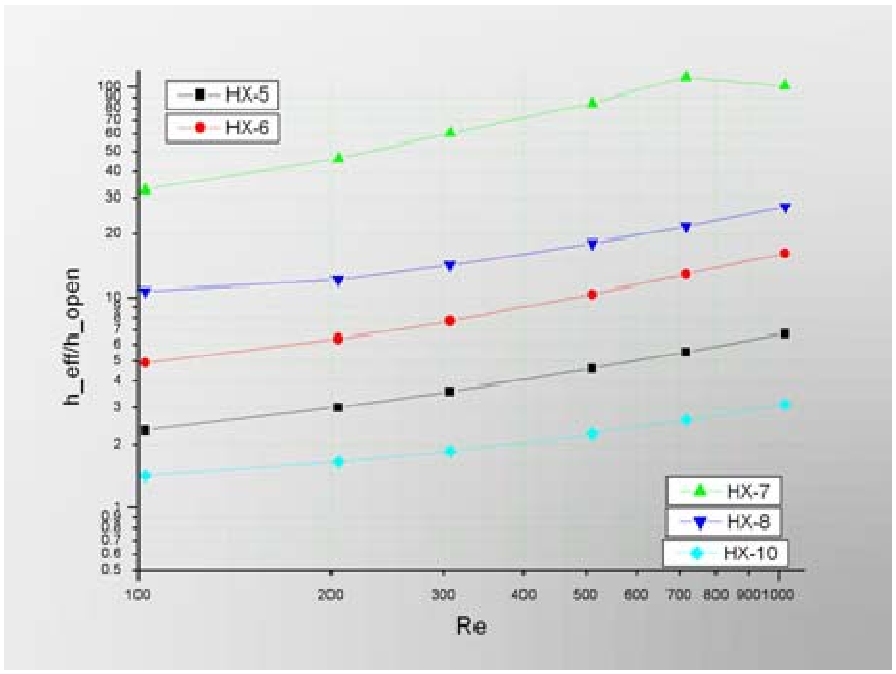

Figure 44. Variation of arrays' effective heat transfer coefficient over the empty duct for HXs 5-8,10

B. NUSSELT NUMBER VARIATION

The variation of Nusselt number with the Reynolds number is shown in figure 45 for the first set of arrays. The trends are not very different compared to the behavior of the average heat transfer coefficient.

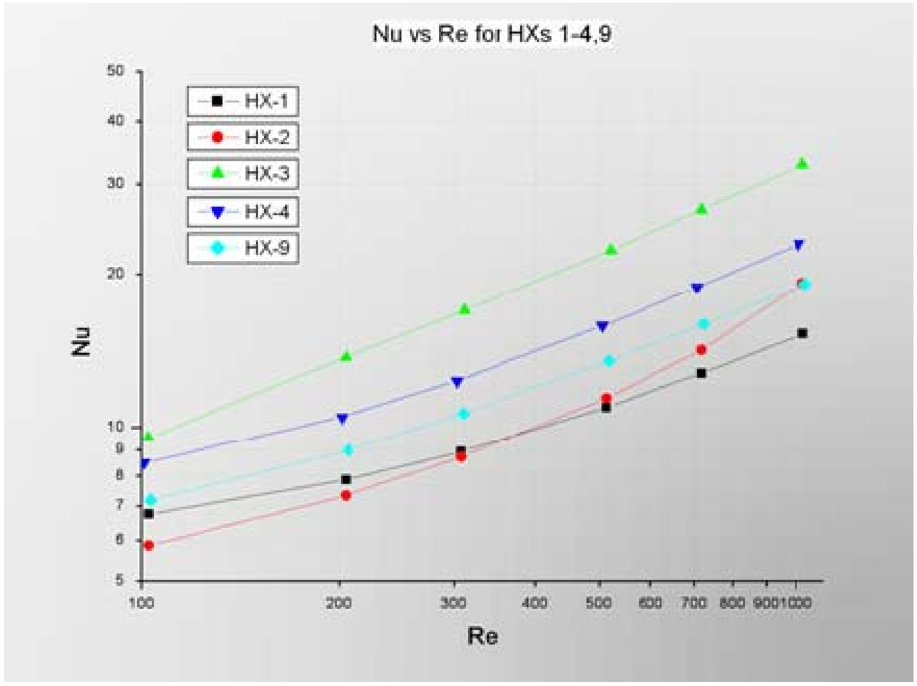

Figure 45. Nusselt number comparison for HXs 1-4,9

The actual relation between the heat exchangers has changed a little because the Nusselt number has been influenced by the hydraulic diameter, as defined in a previous chapter, according to equation 2. This differentiation first concern HX-2, which has moved in a lower scale, and HX-9, which has moved upward relative to HX-1, always compared with the heat transfer coefficient trends. This is valid with the variation of their hydraulic diameter, which for HX-2 with the smaller volume and the same cross sectional area as HX-1, results in a smaller diameter. For HX-9 the reduction of both ratios (X/D and S/D) produced a smaller fractional reduction in the volume than in the cross sectional area, and consequently, the enlargement of the hydraulic diameter. Furthermore, when considering the Nusselt number variation, the opening between the HX- 3 and HX-4 has been decreased, since the hydraulic diameter of 567μm of HX-4, compared to the 307μm of HX-3, appears as an amplification factor for HX-3. This trend is clearer in the second set, where the increase of the H/D ratio increased the heat transfer coefficient for both HXs 7 and 8, but the further increase to the hydraulic diameter for HX-8 ($D_{h,8}$=354μm vs $D_{h,7}$=137μm) dominated and caused not only the gap's total diminishing but also the eighth array's outperformance over the seventh until an Re equal to 300.

By continuing with the exchangers in the second set, as was done for the heat transfer coefficient, the performance curves in figure 46 include the effect of the increase in the H/D relation and the alteration to their trends by our characteristic length, the hydraulic diameter.

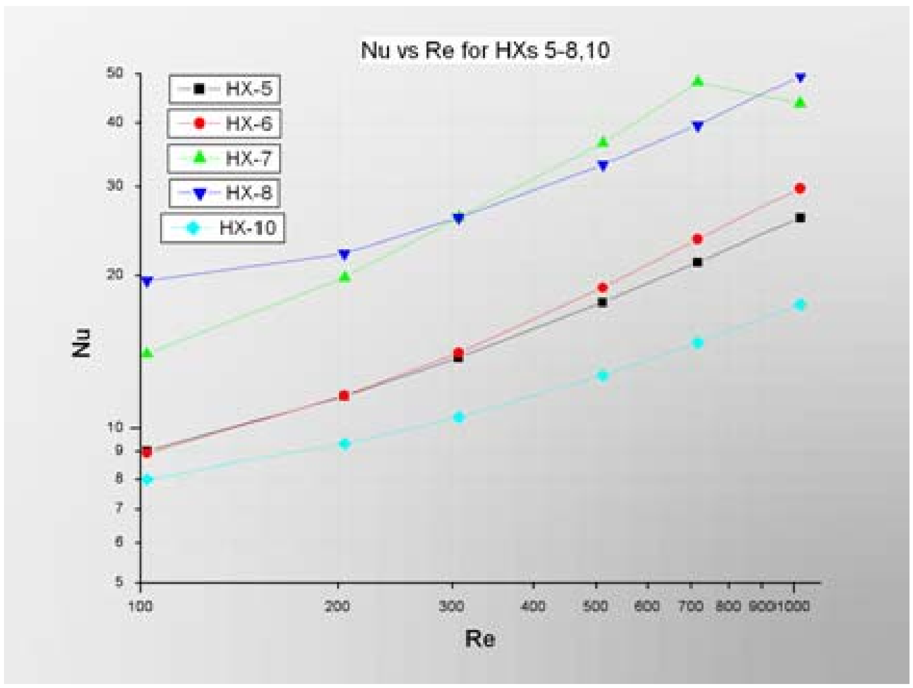

Figure 46. Nusselt number comparison for HXs 5-8,10

In judging all the configurations' performance considering the Nusselt number, against the heat transfer performance of an open channel with a constant surface temperature boundary which produces an average Nu equal to 7.54 (Ref 26), almost all of them attained much higher values for the whole tested range of the Re number. The only exceptions were HX-1 and HX-2, which cross the limit of the constant open channel performance around a Reynolds number of 200.

C. FRICTION FACTOR EFFECTS

The most obvious effect that occurred in the friction factor, in comparing the two sets, was the magnification due to the increase of the H/D fraction that resulted from the reduction of the pin diameter, while keeping the channel height constant. The reduction of the pin diameter caused a decrease in the hydraulic diameter and also a great increase in the average array velocity. However, these two changes were not enough to offset the decrease of total array length and, more significantly the increase in the pressure gradient between the entrance and the exit of the exchanger.

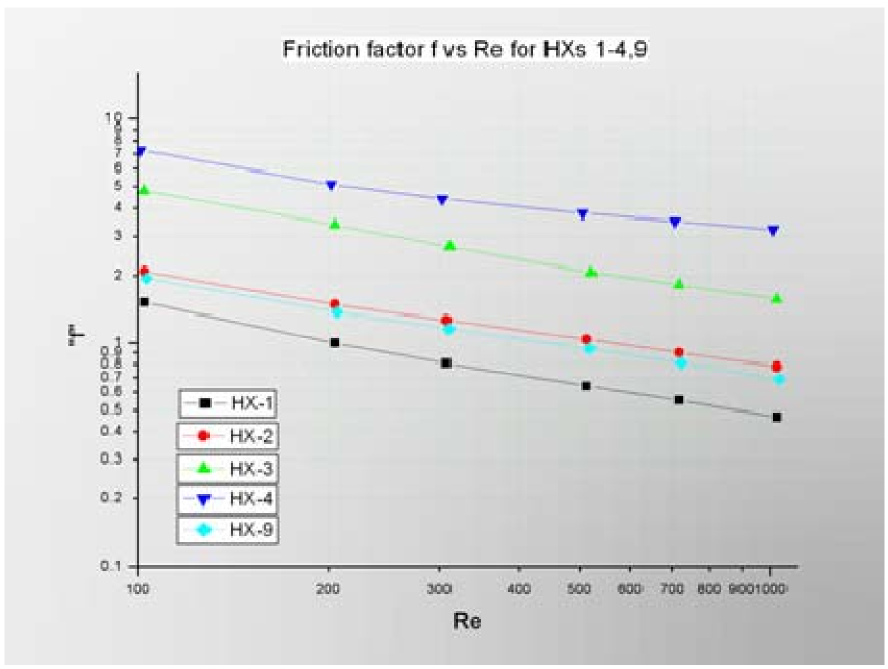

Figure 47. Effect of Reynolds number in friction factor of HXs 1-4,9

Furthermore, for the friction factor, like the other parameters, we note that the amplification due to the alteration of the H/D was not proportional for all the arrays. Thus, this is another proof that the changes to the geometric fractions do not act independently and must be considered together.

If we consider the difference in the effects between HXs-2 and 4, or 6 and 8, since they have the same hydraulic diameter, and thus the same average velocity, the main cause of it, is the great difference between the two differential pressures of the compared arrays. Moreover, this cause is consistent with the theory given that the smaller S/D ratio for HXs-4 and 8 produces a narrower span-wise spacing for the pins and consequently the flow streamlines negotiate a more serpentine path around the pins, which leads to the greater pressure drops. On the other hand in HXs-2 and 6 there's a more direct path and more smooth streamlines, and result in smaller energy amounts being needed to drive the flow through their interior.

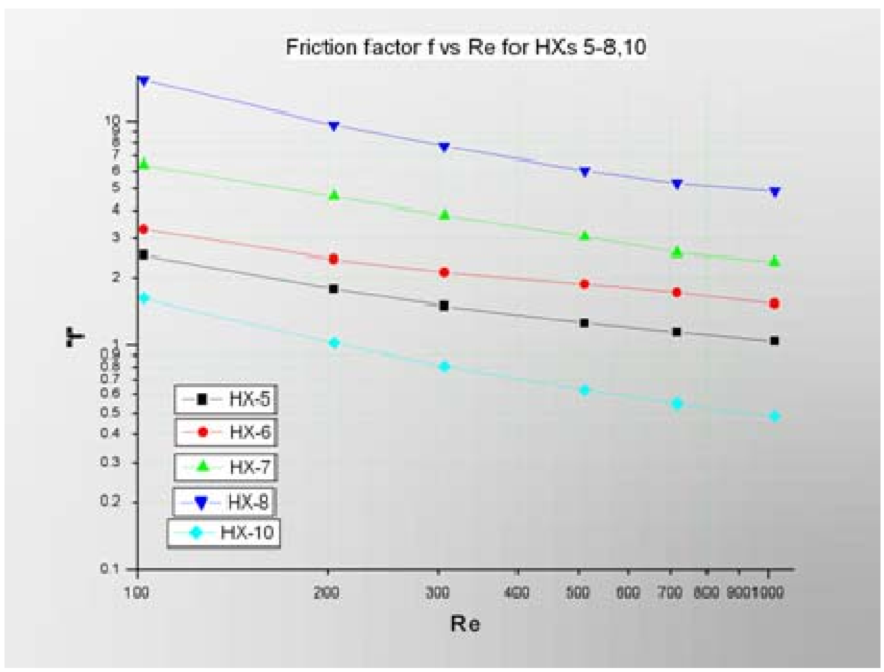

Figure 48. Effect of Reynolds number in friction factor of HXs 5-8,10

Another aspect worth noting is the high friction factor that HXs 4 and 8 produce, especially as compared with HXs-3 and 7. The main reason for that is the dependence on the squared of the average velocity at every Re number and, the increased hydraulic diameter.

By comparing the pressure drop across the inlet and the exit of every configuration, with the pressure drop required from the corresponding dimensions empty of pins duct, to run the flow through it, we get figures 49 and 50. The amount of energy required for the several arrays in order to increase the heat transfer performance shows similar behavior to the corresponding friction factor.

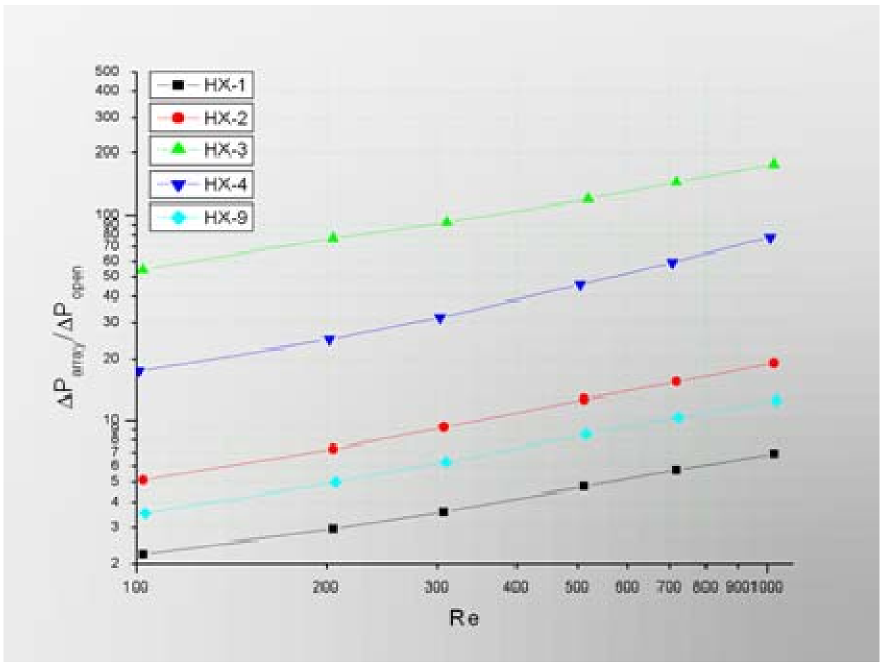

Figure 49. Ratio of HXs 1-4,9 pressure drop over the empty duct case vs. Re

When considering an optimization and a selection process of the most suitable HX for an application, the amount of the pressure drop required for returning the maximum heat transfer performance or the inverse, has to be examined. Thus, HX-7 requires around five times more pressure difference of the increase in heat transfer that provides, HX-8 proved to require six times more, while HX-6 proved to be more economical by demanding three times greater pressure difference than the times that increase the heat transfer when compared to the open duct case.

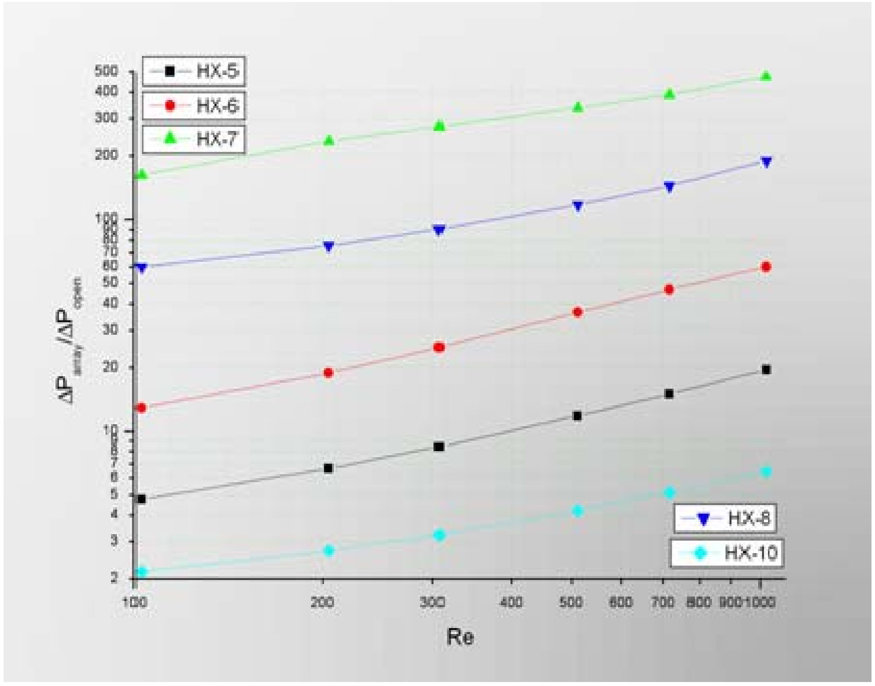

Figure 50. Ratio of HXs 5-8,10 pressure drop over the empty duct case vs. Re

D. MACH NUMBER VARIATION

The deterioration of the heat transfer performance of HX-7 is a very interesting manifestation of Mach number variation. If we also consider the extremely small values of the hydraulic diameter for these micro-scale devices it is obvious that high velocities have to be simulated to provide the desired tested Reynolds numbers.

Recognizing that CFD – ACE is not the most suitable solver for studies that involve Mach numbers over 0.7-0.8 the presented results and effects are rough estimates and must be seen as only adequately accurate in revealing the main trends. A compressible solver like CFD – FASTRAN would be required to resolve shock behavior with greater accuracy but was not used here since it was peripheral to the main study.

However by using the CFD – VIEW, we tried to identify the maximum Mach numbers that occurred in every array and to plot them with respect to the Reynolds number. They are presented in figures 51 and 52. Suitable correlations to define this operational region would be useful in the design process. The coefficients of a power law correlation below are shown in table 8.

$$M = C_1 Re^{C_2} \quad (33)$$

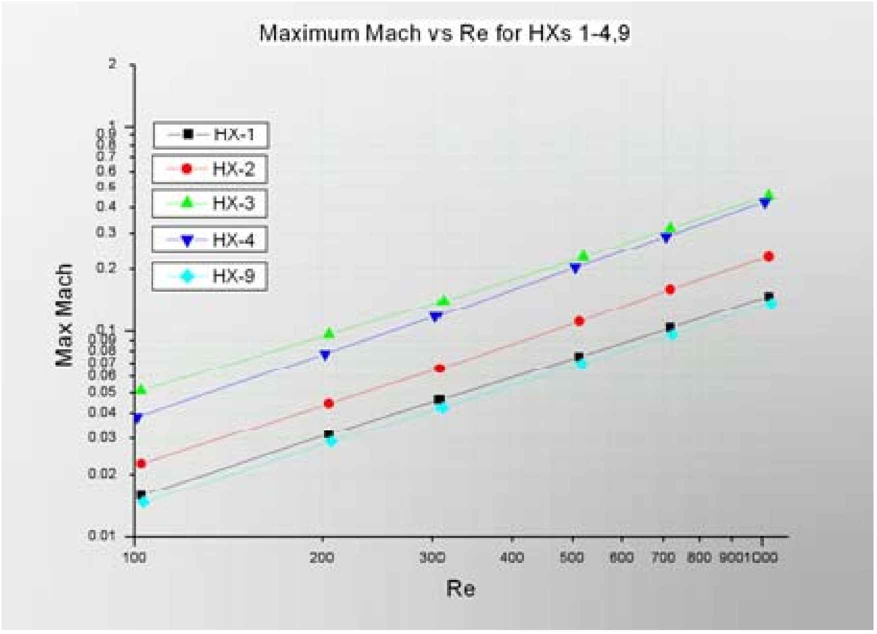

Figure 51. Maximum Mach number variation with Re number for HXs 1-4,9

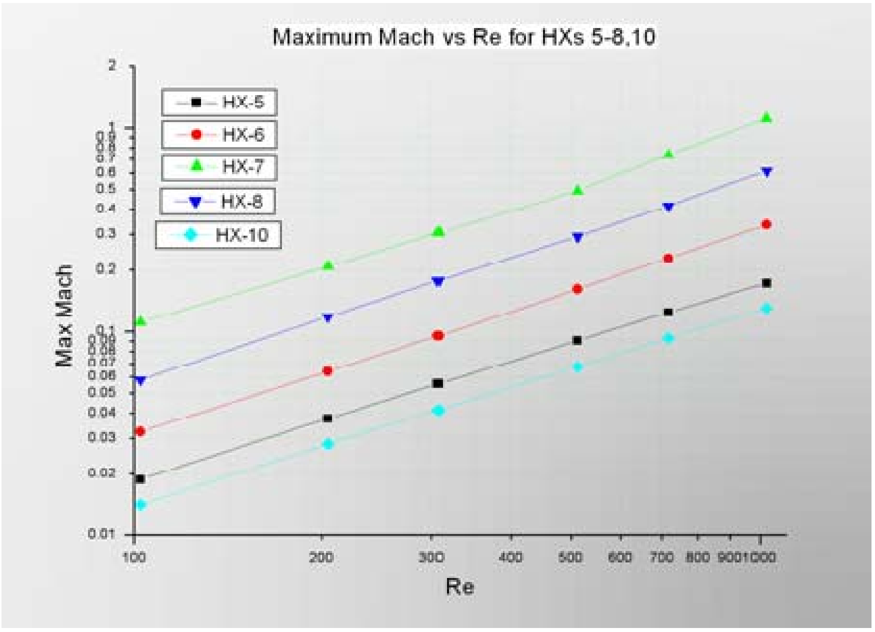

Figure 52. Maximum Mach number variation with Re number for HXs 5-8,10

We have to mention again that these correlations are not intended as an accurate prediction of the flow Mach number, but rather as a rough guess in order to assist in an attempt to avoid any interference with shock waves.

Table 8. Mach number correlations' coefficients

HX #	C_1	C_2
1	0.0002	0.9644
2	0.0002	1.009
3	0.0006	0.9445
4	0.0003	1.0442
5	0.0002	0.9635
6	0.0003	1.0158
7	0.0005	1.0179
8	0.0011	0.991
9	0.0002	0.968
10	0.0002	0.9606

HX-7 demonstrated these shock conditions at the high inlet velocities that the theory dictated for the tested Re numbers and found to have maximum Mach number values of about 1.1. Furthermore, if we consider the inlet velocity of 60m/sec, or the average of 121m/sec, or the maximum value of the fully developed profile of 90m/sec for the corresponding Re equal to 1,000, and the drastic reduction of the available flow area between the pin passageways, shock waves in these nozzles like sections seem unavoidable. The contours of the Mach number and pressure distribution around the throat, illustrated in figure 53, is another indication. We recognize that the coarser unstructured grid around the centerline is not appropriate for capturing the occurring shock conditions.

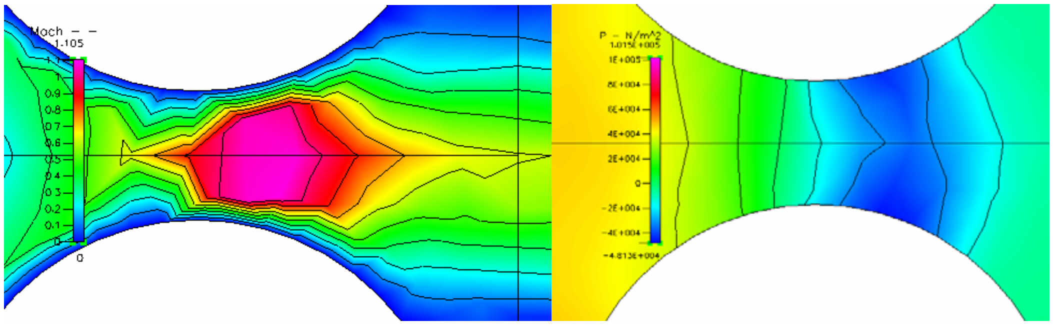

Figure 53. Contour plot of pressure and Mach number distribution in the 4th row of HX-7

In addition, the fact that the critical pressure ratio of 0.528 when a shock can occur is reached is a clear indication. For all these reasons, we are confident that the shock behavior was captured to some degree by ACE and is reflected in a decline in the heat transfer coefficient and in Nusselt number values around a Reynolds number of 1,000.

Bosserman (Ref. 18) observed a very similar condition for HX-3, the denser of the first set in his experimental research. Also HX-3 contains the same area percentage reduction between the pins as HX-7 does. He observed similar decreased performance conditions around a Reynolds number of 1,000 at the same parameters. Figure 54 presents an indication of the variation of Nusselt versus Reynolds number for HX-3 with his data.

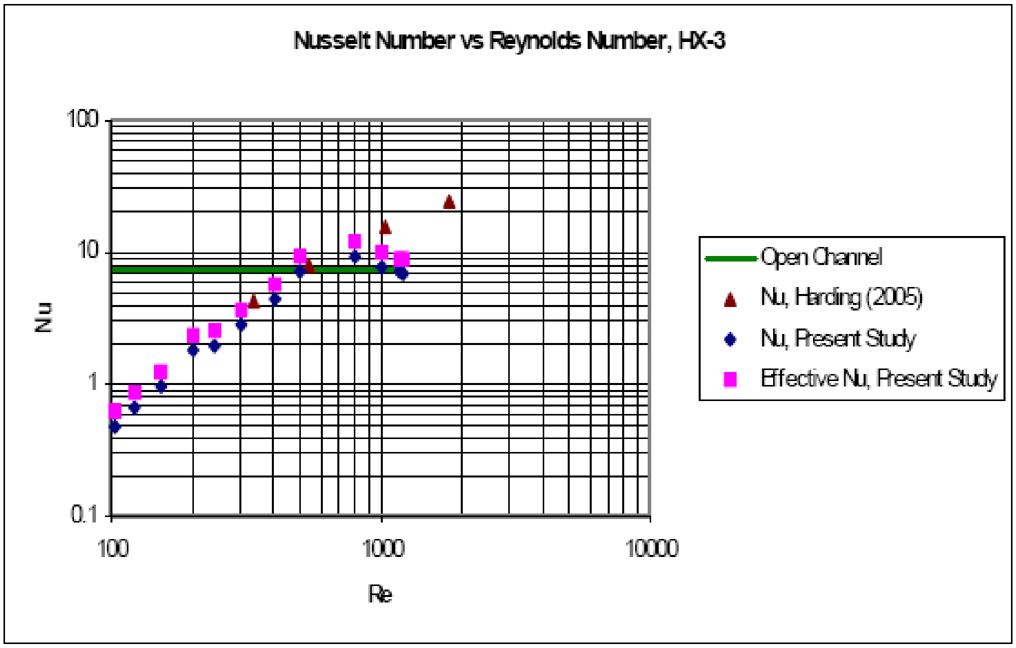

Figure 54. Nu with Re variation for HX-3 [from Bosserman, 2005]

In considering the data in table 9 that provides the required velocities, inlet duct, and average velocities, we concluded that a shock condition must have happened at a smaller Reynolds number than expected, since at a Re equal to 700, the theory gives an inlet velocity of 17m/sec for which it is very difficult for the flow to be chocked under the geometrical features of this array. However, if we consider the blockage affects that Bosserman faced as well, it is very possible that the flow was at higher velocities and that he experienced shock conditions that are consistent with the gathered data.

Table 9. Inlet duct and average array velocities for HX-3 for several Re

$Re_{Dh,ar}$	m_dot_{ar}(kg/s)	U_{ave_ar}(m/s)	V_{in}(m/s)
100	1.5463E-06	5.39	2.68
200	3.0926E-06	10.78	5.36
300	4.6389E-06	16.18	8.05
500	7.7315E-06	26.96	13.41
700	1.0824E-05	37.75	18.77
1000	1.5463E-05	53.92	26.82

E. SLUG VELOCITY PROFILE CONSIDERATIONS

One of our considerations was whether the performance of the heat exchangers would change and if so how much, by applying a more realistic and not fully developed velocity profile as an input boundary. Therefore, the problem changed to a thermal constant surface entry length combined with a flow developing condition. Also it is well known (Ref. 26) that the thermal layer generally develops faster than the velocity boundary layer for fluids with a $Pr < 5$.

Thus, we chose five arrays from both groups, with the smaller and the bigger pin diameter, in order to check the effect of all the spacing ratios, testing them in the new conditions. We removed the entry duct from the model and we applied directly a “slug” constant velocity at the inlet of the exchanger that corresponded to the desired Reynolds number. It is very clear from figure 55 that the performance did not change too much when the slug inlet velocity models were compared with the fully developed velocity profile models. We can observe a slight increase in the heat transfer coefficient at all the ranges of the Reynolds number, with another slight increase for the energy required to drive the flow through the exchanger.

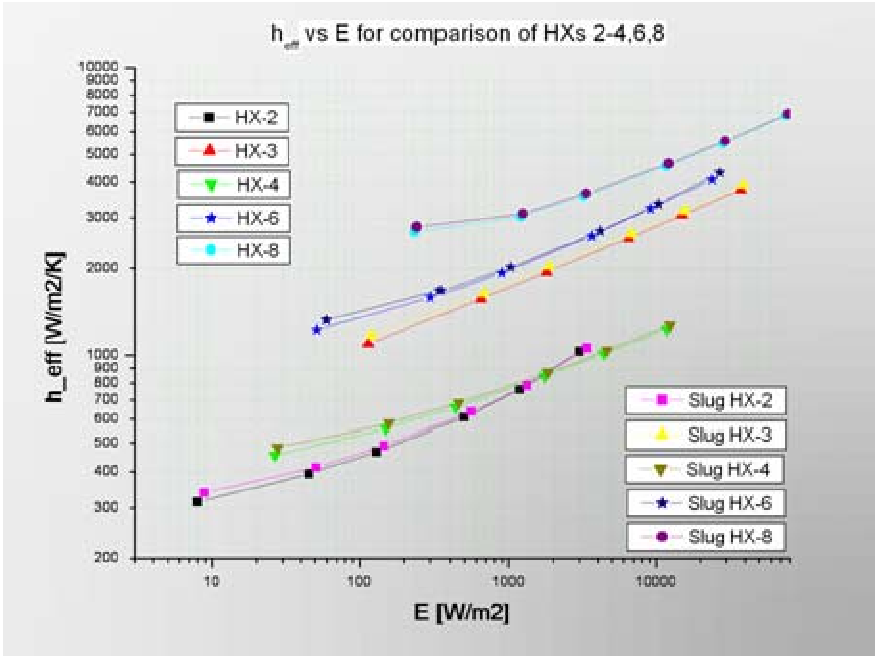

Figure 55. Fully developed and slug velocity profile comparison effect at the HXs 2-4,6,8 for h_{eff} and E

The resulting behavior is consistent with the fluid physics, since from the flow perspective at the initial part of the endwall, the friction gradient will be very high until the flow will be developed relative to the endwall, resulting in increased fluid friction power and also in an enhanced heat transfer performance.

As far as the Nusselt number is concerned, it is higher, especially for the lower x+ values. Also, as the x+ increases, the Nusselt number has to converge to the values of the thermal length only problem, since the effects of the combination of the two developing conditions are diminished. Thermal development is attained when the x+ coordinate reaches values of 0.1.

Table 10. x+ values for HX 2-4,6,8 in Re=100,1000

HX#	D_{h_ar}(m)	L(m)	x+ for Re=100	x+ for Re=1000
2	0.000567	0.00625	0.312	0.031
3	0.000307	0.00250	0.230	0.023
4	0.000567	0.00600	0.299	0.030

6	0.000354	0.00208	0.166	0.017
8	0.000354	0.00200	0.160	0.016

In table 10 we notice that for all the tested exchangers, the thermal development was reached for Re=100, however we are slightly below this point for the higher Reynolds number flow conditions. Thus, we expected the deviation in the Nusselt number between the similar geometrically models compared, to slightly increase as the Reynolds number was increasing, which did not occur.

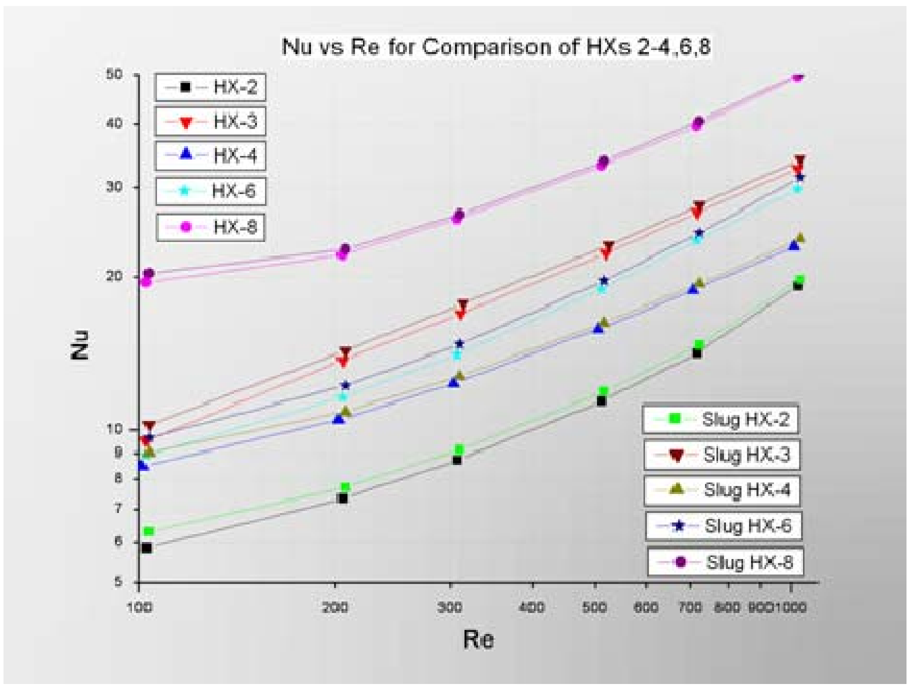

Figure 56. Nusselt number variation for compared velocity profiles in HXs 2-4,6,8

The most probable explanation is that the performance characteristics had changed so little that it was of the order of the simulation accuracy, and we could not identify the above mentioned characteristic behavior. Also we noticed that the selection of the total number of rows for modeling every configuration was consistent with the corresponding x+ values in order to reach a near thermal developed condition, as was explained in the chapter two.

A plot of friction factor with Re in figure 57 helps to compare the role of inlet velocity profile on pressure drop. It is clear that there is very little influence of the velocity profile and noticeable only for HX-2 and HX-6.

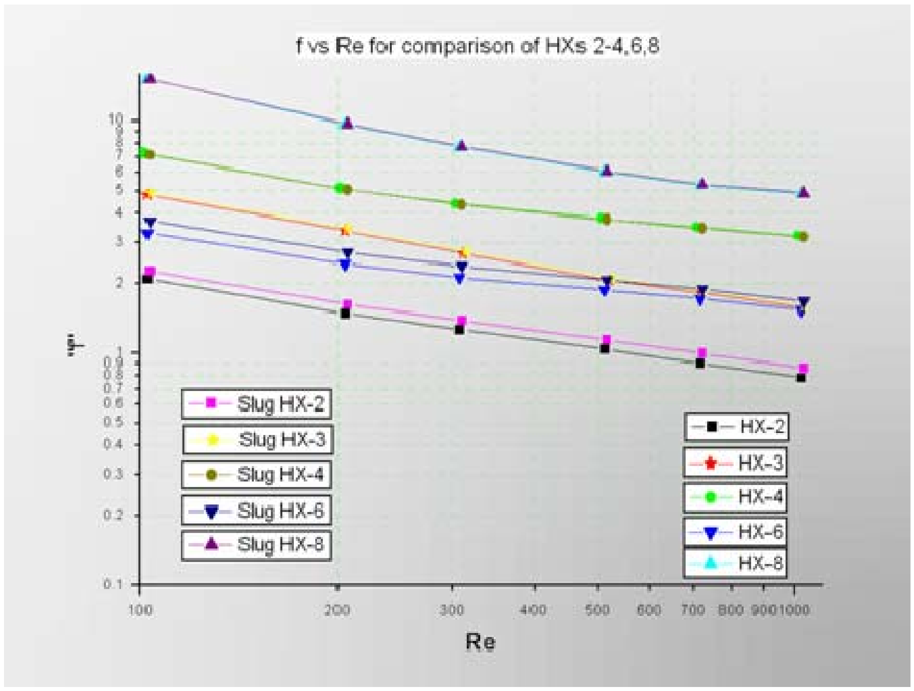

Figure 57. Friction factor variation for compared velocity profiles in HXs 2-4,6,8

The most logical explanation is that for the heat exchangers that provide a larger cross sectional area for the flow, the effects of the change in the inlet velocity profile were more important due to greater interactions with the endwall. In the other configurations, probably the presence of the pins and their dominant "denser" arrangement did not allow great changes in the compared parameters.

THIS PAGE INTENTIONALLY LEFT BLANK

V. CONCLUSIONS AND RECOMMENDATIONS

The objectives of this study were successfully met by computationally simulating the performance of ten micro heat exchangers with varied X/D, S/D, and H/D ratios. The code CFD – ACE was found to be very robust and user-friendly and was used with great confidence for the subsequent computations of the laminar flow regime and the performance maps of the interesting parameters. Most of the significant conclusions have been pointed out during the discussion in each section/chapter.

In summary, we can say that the laminar modeling was shown to be accurate until a Reynolds number of 1,000. At higher values of Re there's a likelihood of transition to turbulence, although the transition value is not constant and is greatly dependent on the geometric configuration of each array.

The ninth and tenth configuration was well enough validated by historical macro-scale and current experimental micro-scale data. Thus, we can conclude that direct application of the macro-scale dimensionless parameters can be performed in the micro-scale dimensional heat exchangers in order to examine the performance of any desired configuration.

Moreover, we noticed that the effects of an alteration of any of the geometric ratios influence the resulting effects of the variation of the other ratios. This was more pronounced for the H/D ratio.

The performance maps of the interesting parameters like the Nusselt number, average and effective heat transfer coefficient, specific fluid friction power, friction factor, and Mach number were also provided for in all the configurations. They can be very useful tools during a design process. The tremendous ability and potential for heat transfer removal, especially for the more packed arrays, has been pointed out and also the extreme fluid power that some of them required.

An examination of the inner part of the compact heat exchanger was conducted, and, mostly, the behavior of the pins compared to the endwall was performed, which proved the great contribution that the pins provide in the total heat transfer removal process.

The desired tested Reynolds number simulations in the micro-scale dimensions required much higher velocities which led to shock wave conditions very early for HX-7, Thus, the computation with varied properties was proved, the best selection. Also the presence of vacuum effects at the exit of some exchangers further enhanced more the choice of the variable properties modeling.

The alteration of the inlet velocity profile that was performed by a constant “slug” velocity profile, in order to inspect the change in the parameters’ trends, did not return any considerable deviation of the initial maps.

For all these reasons, the optimization and the design of micro-scale compact heat exchangers is a complicated process. It must be executed with considerable attention, since one has to consider more physical phenomena than in macro-scale design.

Likewise to get a more total picture of the performance in future work we recommended that the viscous dissipation effects be taken into account in a computational model, in order to check how this negatively affects the output.

Also the examination of configurations with other shape fins that will provide better flow characteristics and will be more effective is emerging, while the difference on the heat transfer performance that the liquids will provide has to be considered.

Finally of a lesser concern is the fact that in some of the exchangers tested (only two to three) for the higher Reynolds number (700 and more for 1,000), the residuals had a periodic pattern. This feature is an indication of unsteadiness, which we recommend should be checked by running an unsteady simulation to inspect any effects on the final performance behavior of the heat exchangers.

THIS PAGE INTENTIONALLY LEFT BLANK

LIST OF REFERENCES

Ref.1 Metzger, D.E., Fan, C.S., Haley, S.W., "Effects of Pin Shape and Array Orientation on Heat Transfer and Pressure Loss in Pin Fin Arrays, Journal of Engineering for Gas Turbines and Power," Vol. 106, 1984, pp. 252-257.

Ref.2 Han, J.C., Dutta, S., and Ekkad, S., "Gas Turbine Heat Transfer and Cooling Technology, Taylor and Francis, 2000.

Ref.3 Stephens, L.S., Kelly, K.W., Kountouris, D., and McLean, J., "A Pin Fin Microheat Sink for Cooling Macroscale Conformal Surfaces Under the Influence of Thrust and Frictional Forces," Journal of Microelectromechanical Systems, Vol. 10, No. 2, pp. 222-231, 2001.

Ref.4 Marques, C., 2003, "Manufacturing and Analysis of a LIGA Heat Exchanger for the Surface of a Tube: A Cooling Simulation of the Leading Edge Region of a Turbine Blade," Ph.D. dissertation, Louisiana State University, Baton Rouge, LA.

Ref.5 VanFossen, G.J., "Heat-Transfer Coefficients for Staggered Arrays of Short Pin Fins, Journal of Engineering for Power," Vol. 104, 1982, pp. 268-274.

Ref.6 Metzger, D.E., Berry, R.A., Bronson, J.P., "Developing Heat Transfer in Rectangular Ducts with Staggered Arrays of Short Pin Fins, ASME Journal of Heat Transfer," Vol. 104, 1982, pp. 700-706.

Ref.7 Hamilton, L.J., "Numerical Analysis of the Performance of a Staggered Cross-Pin Array Heat Exchanger," Naval Postgraduate School, Monterey, California, 2003.

Ref.8 Arora, S.C., and Abdel-Messeh, W., "Pressure Drop and Heat Transfer Characteristics of Circular and Oblong Low Aspect Ratio Pin Fins," AGARD Conference Proceedings, pp.4-1-4-15, 1985.

Ref.9 Chen, Z., Li, Q., Meier, D., and Warnecke, H.J., "Convective Heat Transfer and Pressure Loss in Rectangular Ducts with Drop-Shaped Pin Fins," Heat and Mass transfer, Vol. 33, pp.219-224, 1997.

Ref.10 Chyu, M.K., "Heat Transfer and Pressure Drop for Short Pin-Fin Arrays with Pin-Endwal Fillet," ASME Journal of Heat Transfer, Vol. 112, 1990, pp. 926-932.

Ref.11 Al Dabagh, A. M., and Andrews, G.E., “Pin-Fin Heat Transfer: Contributions of the Wall and the Pin to the Overall Heat Transfer,” ASME Paper No. 92-GT-242, 1992.

Ref.12 Chyu, M.K., Hsing, Y.C., Shih, T.I.P., and Natarajan, V., “Heat Transfer Contributions of Pins and Endwall in Pin-Fin Arrays: Effects of Thermal Boundary Condition Modeling,” ASME J. of Turbomachinery, Vol. 121, pp. 257-263, 1998.

Ref.13 Tahat, M.A., Babus’hag, R.F., Probert, S.D., “Forced Steady-State Convections from Pin-Fin Arrays”, Applied Energy, 1994; 48:335-51.

Ref.14 Tahat, M., Kodah, Z.H., Jarrah, B.A., Probert, S.D., “Heat Transfers From Pin-Fin Arrays Experiencing Forced Convection,” Applied Energy, 2000; 67:419-42.

Ref.15 Li, Q., Chen, Z., Flechtner, U., Warnecke, H.J., “Heat Transfer and Pressure Drop Characteristics in Rectangular Channels with Elliptic Pin Fins,” Int. J. of Heat and Fluid Flow, Vol. 19, pp. 245-250, 1998.

Ref.16 Marques, C., Kelly, K., “Fabrication and Performance of a Pin Fin Micro Heat Exchanger,” ASME Journal of Heat transfer, Vol. 126, pp. 434-444, 2004.

Ref.17 Roussakies, J.C., “An Empirical Study of the Performance of Pin-Fin Micro Heat Exchangers,” Naval Postgraduate School, Monterey, California, 2004.

Ref.18 Bosserman, W.P., “An Empirical Performance Study of Compact Pin-Fin Heat Exchangers,” Naval Postgraduate School, Monterey, California, 2005.

Ref.19 Donahoo, E.E., Camci, C., Kulkarni, A.K., and Belegundu, A.D., “Determination of Optimal Row Spacing for a Staggered Cross-Pin Array in a Turbine Blade Cooling Passage,” Enhanced Heat Transfer, Vol. 8, 2001, pp. 41-53.

Ref.20 Choo, J.S., “Numerical Analysis of the Performance of Staggered Micro Pin-Fin Heat Exchangers,” Naval Postgraduate School, Monterey, California, 2003.

Ref.21 Summers, J., “Empirical Study of a Pin Fin Heat Exchanger in Laminar and Turbulent Flow,” Naval Postgraduate School, Monterey, California, 2003.

Ref.22 White, F.M., Fluid Mechanics, McGraw-Hill, Inc., 4th Ed., 1999.

Ref.23 Zukauskus, A., “Heat Transfer from Tubes in Crossflow,” Advances in Heat Transfer, Vol. 8, 1972, pp. 93-160.

Ref.24 CFD – ACE+ User Documentation-Manual, 2004

Ref.25 Versteeg, H.K., Malalasekera, W., “An Introduction to Computational Fluid Dynamics,” the Finite Volume Method, Pearson, Harlow, England, 1995.

Ref.26 Kays, W.M., and Crawford, M.E., “Convective Heat and Mass Transfer,” 3rd Ed., McGraw-Hill, New York, 1993.

Ref.27 Kays, W.M., and London, A.L., “Compact Heat Exchangers,” 3rd Ed., McGraw-Hill, New York, 1984

Ref.28 Incropera, F.P. and DeWitt, D.P., “Introduction to Heat Transfer,” John Wiley and Sons, New York, NY, 4th Ed., 1996

Ref.29 CFD – ACE+ Modules Documentation-Manual, 2004

Ref.30 Chien, K.Y., “Prediction of Channel and Boundary-Layer Flows with a Low Reynolds Number Turbulence Model,” AIAA Journal 20.1 (1982):33-38.

THIS PAGE INTENTIONALLY LEFT BLANK

INITIAL DISTRIBUTION LIST

1. Defense Technical Information Center
   Ft. Belvoir, Virginia

2. Dudley Knox Library
   Naval Postgraduate School
   Monterey, California

3. Professor Ashok Gopinath
   Naval Postgraduate School
   Monterey, California

4. Professor Jose Sinibaldi
   Naval Postgraduate School
   Monterey, California

5. LTJG Sotirios Dimas, Hellenic Navy
   Naval Postgraduate School
   Monterey, California